Tectonophysics

Compaction-driven melt extraction and accumulation in a slow-spreading oceanic crust: microstructures of olivine gabbros from the Atlantis Bank(IODP Hole U1473A, SWIR)
--Manuscript Draft--

Corresponding Author:	Carlotta Ferrando, Ph.D. University of Pavia: Universita degli Studi di Pavia Pavia, ITALY
First Author:	Carlotta Ferrando, Ph.D.
Order of Authors:	Carlotta Ferrando, Ph.D.
	Valentin Basch, Ph.D.
	Benoit Ildefonse
	Jeremy Deans
	Alessio Sanfilippo
	Barou Fabrice
	France Lyderic

Abstract:	The exposure of gabbroic sequences at Oceanic Core Complexes (OCC) along ultraslow-to slow-spreading ridges permits the study of the processes forming the lower oceanic crust. On top of the Atlantis Bank OCC along the ultraslow-spreading Southwest Indian Ridge, IODP Expedition 360 drilled HoleU1473A, mainly composed of primitive olivine gabbros interspersed with more evolved Ti-Fe oxide-bearing gabbros and minor felsic veins. These rocks record a complex history of protracted magmatism during continuous uplift and deformation of the gabbroic sequence. Extensive crystal-plastic deformation is dominantly recorded in the shallower sections of the drillhole, whereas the deeper sections better preserve primary magmatic features. We focus on microstructures, including intra-crystalline deformation of rock-forming minerals, and plagioclase crystallographic preferred orientations of olivine gabbros lacking evidence for exhumation-related crystal plastic deformation, to gain insights on the relationship between compaction, melt migration and melt accumulation during the early magmatic history of this section of lower oceanic crust. Olivine gabbros are characterized by ubiquitous grain-size variations, from coarse- to fine-grained intervals. Minerals in coarse-grained intervals show intra-crystalline deformation, while fine-grained crystals lack internal strain. Bent coarse-grained plagioclase associated with weak magmatic foliation and lack of lineation suggest that the coarse-grained intervals were deformed under compaction. On the other hand, crystallographic preferred orientations of undeformed fine-grained plagioclase show weak lineations, likely indicative of non-coaxial strain. We infer that the coarse-grained intervals underwent ongoing compaction from the stage of olivine + plagioclase ± clinopyroxene crystal mush to the melt-poor stage, and that this process likely aided melt extraction and accumulation in discrete melt-rich zones where crystals orientated in the direction of magmatic flow. Crystallization of melts in the melt-rich zones ultimately formed the fine-grained intervals at different depths in Hole U1473A. This indicates that processes of compaction can lead to local chemical and grain-size heterogeneities in a lower crustal section.

	Expert in microstructures of gabbroic rocks
	Karoly Hidas k.hidas@igme.es Expert in microstructures
	Mary-Alix Kaczmarek kaczmarek@get.omp.eu Expert in microstructures

UNIVERSITÀ DEGLI STUDI DI PAVIA
DIPARTIMENTO DI SCIENZE DELLA TERRA E DELL'AMBIENTE

Carlotta Ferrando
Post-doc Researcher in igneous petrology
Department of Earth and Environmental Sciences - University of Pavia
Via Ferrata 1 - 27100 Pavia
carlotta.ferrando@unipv.it

Pavia, 18/01/2021

To: Prof. Philippe Agard
Editor in Charge of the *Adolphe Nicolas Special Issue "Deformation processes in the ductile crust and mantle, seismic anisotropy, and ocean ridge dynamics"* in Tectonophysics

Dear Prof. Agard,

Please find enclosed the manuscript entitled "**Compaction-driven melt extraction and accumulation in a slow-spreading oceanic crust: microstructures of olivine gabbros from the Atlantis Bank (IODP Hole U1473A, SWIR)**, by

Carlotta Ferrando, Valentin Basch, Benoit Ildefonse, Jeremy Deans, Alessio Sanfilippo, Fabrice Barou, Lydéric France

that we wish to submit for publication on **Tectonophysics,** *Adolphe Nicolas Special Issue "Deformation processes in the ductile crust and mantle, seismic anisotropy, and ocean ridge dynamics"*.

    Sequences of lower oceanic crust exposed at Oceanic Core Complexes (OCC) along ultraslow- to slow-spreading ridges record a complex history of protracted magmatism during continuous uplift and deformation of the gabbroic rocks. Extensive crystal-plastic deformation commonly overprints pre-existing magmatic fabrics, thus challenging our study of magmatic processes. Despite this, we here were able to select unique samples from the Atlantis Bank OCC preserving magmatic features and lacking evidence for exhumation-related crystal plastic deformation, to better constrain the role of compaction on melt migration through the lower oceanic crust. We provide microstructural constraints of compaction, such as bending of plagioclase, minerals intra-crystalline deformation coupled with low BA-indices pointing to the development of weak foliation with no lineation. We document that compaction aided melt extraction from a pre-existing coarse-grained crystal mush, and accumulation of melts into discrete zones where fine-grained olivine gabbros formed. We also infer that compaction led to local but ubiquitously present grain-size variations, but did not control the large scale melt migration process; the latter was likely driven by melt buoyancy.

    Because Adolphe Nicolas' early works focus on rock deformation processes, and particularly on deformation in presence of melt, we believe that this work would honor his key findings on the architecture and building of the oceanic crust by bringing further understanding on processes driving melt migration through the slow-spreading oceanic crust.

    Sincerely,

Carlotta Ferrando

Compaction-driven melt extraction and accumulation in a slow-spreading oceanic crust: microstructures of olivine gabbros from the Atlantis Bank (IODP Hole U1473A, SWIR)

Carlotta Ferrando[1,2,*], Valentin Basch[2], Benoit Ildefonse[3], Jeremy Deans[4], Alessio Sanfilippo[2], Fabrice Barou[3], Lydéric France[1]

[1] Université de Lorraine, CNRS, CRPG, Nancy, France

[2] Dipartimento di Scienze della Terra e dell'Ambiente, Università degli Studi di Pavia, Pavia, Italy.

[3] Géosciences Montpellier, Université de Montpellier, CNRS, Montpellier, France.

[4] School of Biological, Environmental, and Earth Sciences, University of Southern Mississippi, MS, United States.

Abstract

The exposure of gabbroic sequences at Oceanic Core Complexes (OCC) along ultraslow- to slow-spreading ridges permits the study of the processes forming the lower oceanic crust. On top of the Atlantis Bank OCC along the ultraslow-spreading Southwest Indian Ridge, IODP Expedition 360 drilled Hole U1473A, mainly composed of primitive olivine gabbros interspersed with more evolved Ti-Fe oxide-bearing gabbros and minor felsic veins. These rocks record a complex history of protracted magmatism during continuous uplift and deformation of the gabbroic sequence. Extensive crystal-plastic deformation is dominantly recorded in the shallower sections of the drillhole, whereas the deeper sections better preserve primary magmatic features. We focus on microstructures, including intra-crystalline deformation of rock-forming minerals, and plagioclase crystallographic preferred orientations of olivine gabbros lacking evidence for exhumation-related crystal plastic deformation, to gain insights on the relationship between compaction, melt migration and melt accumulation during the early magmatic history of this section of lower oceanic crust. Olivine gabbros are characterized by ubiquitous grain-size variations, from coarse- to fine-grained intervals. Minerals in coarse-grained intervals show intra-crystalline deformation, while fine-grained crystals lack internal strain. Bent coarse-grained plagioclase associated with weak magmatic foliation and lack of lineation suggest that the coarse-grained intervals were deformed under compaction. On the other hand, crystallographic preferred orientations of undeformed fine-grained plagioclase show weak lineations, likely indicative of non-coaxial strain. We thereby infer that the coarse-grained intervals underwent ongoing compaction from the stage of olivine + plagioclase ± clinopyroxene crystal mush to the melt-poor stage, and that this process likely aided melt extraction and accumulation in discrete melt-rich zones where crystals orientated in the direction of magmatic flow. Crystallization of melts in the melt-rich zones ultimately formed the fine-grained intervals at different depths in Hole U1473A. This indicates that processes of compaction can lead to local chemical and grain-size heterogeneities in a lower crustal section.

Compaction-driven melt extraction and accumulation in a slow-spreading oceanic crust: microstructures of olivine gabbros from the Atlantis Bank (IODP Hole U1473A, SWIR)

Carlotta Ferrando[1,2,*], Valentin Basch[2], Benoit Ildefonse[3], Jeremy Deans[4], Alessio Sanfilippo[2], Fabrice Barou[3], Lydéric France[1]

[1] Université de Lorraine, CNRS, CRPG, Nancy, France

[2] Dipartimento di Scienze della Terra e dell'Ambiente, Università degli Studi di Pavia, Pavia, Italy.

[3] Géosciences Montpellier, Université de Montpellier, CNRS, Montpellier, France.

[4] School of Biological, Environmental, and Earth Sciences, University of Southern Mississippi, MS, United States.

Highlights

- We document first microstructural constraints of compaction in slow-spread gabbros;

- Deformed coarse-grained olivine gabbros developed weak foliation during compaction;

- Undeformed fine-grained intervals developed lineation during melt accumulation;

- Compaction led to the local but ubiquitous chemical and grain-size heterogeneities;

- Large scale melt migration at the Atlantis Bank was mostly driven by melt buoyancy.

1 **Compaction-driven melt extraction and accumulation in a slow-spreading**
2 **oceanic crust: microstructures of olivine gabbros from the Atlantis Bank**
3 **(IODP Hole U1473A, SWIR)**

4 Carlotta Ferrando[1,2,*], Valentin Basch[2], Benoit Ildefonse[3], Jeremy Deans[4], Alessio Sanfilippo[2],
5 Fabrice Barou[3], Lydéric France[1]

6 [1] Université de Lorraine, CNRS, CRPG, Nancy, France
7 [2] Dipartimento di Scienze della Terra e dell'Ambiente, Università degli Studi di Pavia, Pavia, Italy.
8 [3] Géosciences Montpellier, Université de Montpellier, CNRS, Montpellier, France.
9 [4] School of Biological, Environmental, and Earth Sciences, University of Southern Mississippi, MS, United States.

10

11 ## Abstract

12 The exposure of gabbroic sequences at Oceanic Core Complexes (OCC) along ultraslow- to
13 slow-spreading ridges permits the study of the processes forming the lower oceanic crust. On
14 top of the Atlantis Bank OCC along the ultraslow-spreading Southwest Indian Ridge, IODP
15 Expedition 360 drilled Hole U1473A, mainly composed of primitive olivine gabbros
16 interspersed with more evolved Ti-Fe oxide-bearing gabbros and minor felsic veins. These
17 rocks record a complex history of protracted magmatism during continuous uplift and
18 deformation of the gabbroic sequence. Extensive crystal-plastic deformation is dominantly
19 recorded in the shallower sections of the drillhole, whereas the deeper sections better preserve
20 primary magmatic features. We focus on microstructures, including intra-crystalline
21 deformation of rock-forming minerals, and plagioclase crystallographic preferred orientations
22 of olivine gabbros lacking evidence for exhumation-related crystal plastic deformation, to gain
23 insights on the relationship between compaction, melt migration and melt accumulation during
24 the early magmatic history of this section of lower oceanic crust. Olivine gabbros are
25 characterized by ubiquitous grain-size variations, from coarse- to fine-grained intervals.
26 Minerals in coarse-grained intervals show intra-crystalline deformation, while fine-grained
27 crystals lack internal strain. Bent coarse-grained plagioclase associated with weak magmatic
28 foliation and lack of lineation suggest that the coarse-grained intervals were deformed under
29 compaction. On the other hand, crystallographic preferred orientations of undeformed fine-
30 grained plagioclase show weak lineations, likely indicative of non-coaxial strain. We thereby
31 infer that the coarse-grained intervals underwent ongoing compaction from the stage of olivine
32 + plagioclase ± clinopyroxene crystal mush to the melt-poor stage, and that this process likely
33 aided melt extraction and accumulation in discrete melt-rich zones where crystals orientated in
34 the direction of magmatic flow. Crystallization of melts in the melt-rich zones ultimately
35 formed the fine-grained intervals at different depths in Hole U1473A. This indicates that
36 processes of compaction can lead to local chemical and grain-size heterogeneities in a lower
37 crustal section.

1. Introduction

A thick (2 km) section of magmatic lower oceanic crust is exposed at the Atlantis Bank Oceanic Core Complex (OCC), representing one of the best studied examples of ultraslow-spreading oceanic crust in the world. The vertical structure of the Atlantis Bank gabbroic sequence was interpreted as resulting from multiple melt injections forming ephemeral crystal mush bodies of ~400 m maximum thickness (Natland and Dick, 2001, 2002; Dick et al., 2000, 2019a,b; MacLeod et al., 2017; Boulanger et al., 2020) that cooled at relatively rapid rates of ~0.005 °C/yr (John at al., 2004; Coogan et al., 2007).

Single bodies of crystallized crystal mush were identified by upward chemically differentiated units of 200 to 400 m thickness (Dick et al., 2000; Natland and Dick, 2002). These chemical trends were defined using bulk-rock (Natland and Dick, 2002) and mineral chemical compositions (mainly Mg# and Cr_2O_3 in clinopyroxene; Boulanger et al., 2020; Ferrando et al., in revision, 2021; Zhang et al., 2020) progressively evolving towards the top of each magmatic section. To form these chemical trends, melts must have migrated upward as they progressively differentiated within the crystal mushes. Porous melt migration through the Atlantis Bank lower oceanic crust has been described at all scales. Sanfilippo et al. (2020) described the occurrence of a cm-scale 'compositional band' in an apparently homogeneous sample of Atlantis Bank olivine gabbro. They interpreted this band as a record of cryptic melt migration through a primitive crystal mush. At the scale of a single crystal mush reservoir (~300 m thick), Boulanger et al. (2020) proposed that upward melt mobilization by porous flow facilitated the collection of melts from the deepest portions of a gabbroic mush, composed of stacked sills, to an overlying crystal mush constituting the upper half of the reservoir. Also, considering the reconstructed vertical structure of the Atlantis Bank OCC, the increasing modal abundance of oxide gabbros toward the top of the oceanic crustal sequence further suggests melt migration of progressively evolving intercumulus melts (Dick et al., 2000; Natland and Dick, 2001; Zhang et al., 2020).

Porous melt migration has been invoked as a magmatic process playing a major role in the generation of lower oceanic crusts (e.g., Coogan et al., 2000; Lissenberg et al., 2013, 2019; Leuthold et al., 2014; Sanfilippo et al., 2015; Basch et al., 2018, 2019; Ferrando et al., 2018; Dick et al., 2019a; Boulanger et al., 2020; Rampone et al., 2020; Zhang et al., 2020), and as a process capable to modify melts that possibly contribute to erupted MORBs (Lissenberg and Dick, 2008). In crystal mushes, because the density of the melt is lower than the fractionated crystals, the positive buoyancy of melts can drive their upward migration (McKenzie, 1984;

2

73   Lissenberg et al., 2019). Melt transport can be also aided by compaction during the early stages

74   (i.e., crystal mush stages) of magma crystallization (e.g., Nicolas, 1992) as commonly inferred

75   in both oceanic (e.g., Natland and Dick, 2001; VanTongeren et al., 2015; Brown et al., 2019;

76   Lissenberg et al., 2019; Zhang et al., 2020) and continental environments (e.g., Meurer and

77   Boudreau, 1998; Namur et al., 2015; Holness et al., 2017; Bertolett et al., 2019). Compaction

78   of crystal piles may result from coaxial strain (Nicolas, 1992), and has been well documented

79   in Layered Mafic Intrusions by the occurrence of bent and interlocked crystals of plagioclase,

80   together with strong plagioclase shape preferred orientation (e.g., Meurer and Boudreau, 1998;

81   Holness et al., 2017; Bertolett et al., 2019).

82   At slow-spreading ridges, compaction of gabbroic sequences has been invoked as the

83   process driving melt migration and generating the upward chemical trends in single crystal

84   mush bodies (e.g., Natland and Dick, 2001; Lissenberg et al., 2019; Zhang et al., 2020).

85   However, *(i)* compaction of the crystal pile has been merely inferred from plastic deformation

86   of plagioclase crystals only, and *(ii)* the strength and efficiency of compaction to induce melt

87   transport are poorly constrained. The typical coarse-grained textures of oceanic gabbros

88   impede the analyses of a statistically significant number of grains (in a single thin section) to

89   obtain reliable microstructural quantifications. Additionally, slow- to ultraslow-spreading

90   oceanic crust is mainly studied at OCC where crystal-plastic deformation related to detachment

91   faulting commonly overprints primary magmatic fabrics. This strongly challenges sampling of

92   pristine gabbros recording magmatic processes, explaining the poorly documented symmetry

93   of magmatic fabrics at slower-spreading ridges (Cheadle and Gee, 2017).

94   In this contribution, we provide detailed microstructural analyses of olivine gabbros from

95   the *in situ* section of ultraslow-spreading oceanic crust cored in IODP Hole U1473A at the

96   Atlantis Bank OCC. Our sample suite was selected from the deepest section of the hole where

97   minor crystal-plastic deformation overprint is recorded, and primary magmatic features are

98   preserved. Electron Backscattered Diffraction (EBSD) allows us to quantify grain deformation

99   and mineral fabric orientation, strength, and symmetry. Such microstructural quantifications

100 were determined for both coarse- and fine-grained olivine gabbros. EBSD analyses of fine-

101 grained intervals permit to define Crystallographic Preferred Orientations of plagioclase from

102 an ultraslow-spreading crust, and to overcome the poor statistics related to the small number

103 of grains measured in coarse-grained samples. Microstructural analyses are presented here and

104 are used to *(i)* constrain the extent of compaction in the Atlantis Bank lower oceanic crust, and

105 *(ii)* assess the control of compaction on melt extraction from the crystal mush. In a recent

106 geochemical study on the same sample suite, we showed that the melt extracted from the crystal

107 mush segregated in discrete melt-rich zones that ultimately crystallized the fine-grained olivine
108 gabbro cumulates ubiquitously observed throughout Hole U1473A (Ferrando et al., in
109 revision). Here, we investigate the ability of compaction to accumulate melts in these discrete
110 zones.

111

2. The Atlantis Bank and IODP Hole U1473A

113   The Atlantis Bank consists of a ~5000 m-high dome covering an area ~37 km-long and
114 ~30 km-wide (e.g., Dick et al., 1991a; Baines et al., 2003; Hosford et al., 2003). It is located at
115 the inside corner of the intersection of the Atlantis II transform and the ultraslow-spreading
116 SWIR (57°E; Fig. 1a; average spreading rate 14 mm/yr; Dick et al., 1991a). The Atlantis Bank
117 OCC lies on the high transverse ridge that runs parallel to the transform valley and that was
118 created by a 7.5 Myr long transtension phase on the Atlantis II Transform fault due to a
119 spreading direction change at ~19.5 Myr. Transtension substantially uplifted and shifted the
120 Atlantis Bank to its present-day location ~93 km south of the SWIR axis (Fig. 1a; e.g., Dick et
121 al., 1991a; Baines et al., 2007, 2008; Palmiotto et al., 2013).

122   The Atlantis Bank OCC exposes lower oceanic crust and upper mantle denuded by the
123 continuous exhumation event (review in Dick et al., 2019a). Site surveys, geological mapping
124 and drilling (e.g., Dick et al., 1991b, 2000; Pettigrew et al., 1999; MacLeod et al., 1998, 2017;
125 Arai et al., 2000; Matsumoto et al., 2002) revealed that the uplifted lower crust is composed of
126 massive gabbros (dominantly olivine gabbro), emplaced by continuous magmatic activity over
127 ~3 Myr (from ~13.4 to ~10.5 Myr) at approximately 5-6 km-depth beneath the ridge axis
128 (Baines et al., 2008; Rioux et al., 2016). The >4 km-thick magmatic crust estimated in this
129 region (e.g., Minshull et al., 1998) is exceptional for the overall thin and discontinuous lower
130 oceanic crust observed along the SWIR (e.g., Cannat et al., 1999, 2006; Muller et al., 1999);
131 this was attributed to local high melt supply from an unusual portion of fertile mantle (Yu and
132 Dick, 2020). The gabbroic massif was drilled on top of the dome in two ODP Holes 735B and
133 1105A, and the recent IODP Hole U1473A. Overall, the stratigraphy of the three Holes
134 documents adcumulate gabbros showing various 200m to 450m-thick major igneous units
135 depicted by upward decrease in bulk Mg#, Ca#, and Cr and Ni concentrations (Fig. 1b; Dick
136 et al., 2000, 2019a; MacLeod et al., 2017).

137   IODP Hole U1473A (IODP Expedition 360; MacLeod et al., 2017; Dick et al., 2019b)
138 penetrated ~810 meters below sea floor (mbsf), sampling mainly olivine gabbros (76.5 %), less

abundant disseminated-oxide gabbro (containing 1–2% oxide; 9.5% of recovery), oxide gabbro (>5% oxide; 7.5% of recovery), gabbro (sensu stricto; 5% of recovery), and minor felsic veins (1.5%) (Fig. 1b). The cored oceanic crustal section is characterized by a ~560-m thick zone, from ~15 to 585 mbsf (Fig. 1b), with frequent crystal-plastic deformation overprinting the primary magmatic fabrics. Extensive crystal-plastic deformation is observed throughout the Hole, with local ultramylonites mostly present within the uppermost ~300 m. The intensity of crystal plastic deformation decreases downhole, where magmatic features are best preserved (MacLeod et al., 2017; Zhang et al., 2020). Accordingly, primary magmatic fabrics (MF) are identifiable in ~40% of the Hole with the majority of gabbroic rocks displaying random orientation of primary igneous minerals (MF = 0, Fig. 1b), while discrete intervals of about 80 cm thickness maximum are characterized by weak (MF = 1) to moderate (MF = 2) MF defined by the shape preferred orientation (SPO) of elongated laths of euhedral to subhedral tabular plagioclase (Pettigrew et al., 1999).

Olivine gabbros display highly variable mineral grain-size ranging from fine- and medium- (0.2–1.5 mm) to coarse-grained crystals (2-15 mm) (Fig. 1b). Grain-size contacts can be related to local intense crystal-plastic deformation (sheared contacts in Fig.2a), leading to extensive grain-size reduction after dynamic recrystallization. It is plausible that grain-size reduction at sheared contacts occurs in pre-existing, primary, fine-grained intervals. Where gabbros are not plastically deformed, grain-size contacts are of magmatic origin, and thus preserve their primary characteristics (Fig. 2b). Primary magmatic contacts between intervals of different grain sizes are commonly observed (121 contacts logged during IODP Expedition 360; MacLeod et al., 2017; one contact on average every ~4 m of recovered core) and were identified throughout Hole U1473A at all depths (Fig. 1b). Grain-size contacts are mostly irregular and "patchy", i.e. showing coarse-grained domains included into a fine-grained matrix, with variable thickness of fine- (or medium-) and coarse-grained intervals (Fig. 2b; MacLeod et al., 2017).

Shipboard bulk rock analyses highlighted three principal chemical units each showing upward chemical differentiation (Fig. 1b), which are separated by two chemical discontinuities at ~60–90 mbsf and ~350 mbsf (Fig. 1b; MacLeod et al. 2017). In the deepest chemical unit of Hole U1473A, within the depth interval 500-800 mbsf (below the 'no recovery' interval; Fig. 1), the 96% recovery sampled olivine gabbros showing minor crystal-plastic overprint. These olivine gabbros commonly preserve their primary magmatic textures and grain-size variations and thus represent the best candidates to investigate the primary magmatic fabric.
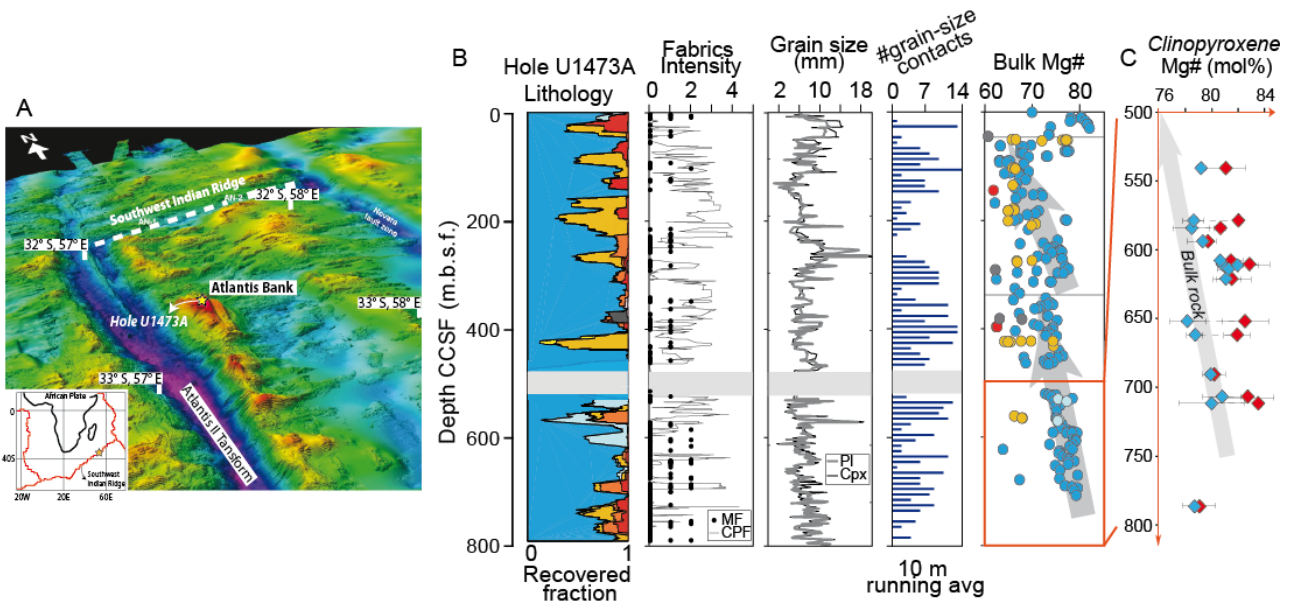
Figure 1: (A) Location of the Atlantis Bank OCC and of IODP Hole U1473A drilled during Expedition 360 on its flat top (modified after MacLeod et al., 2017). (B) Downhole lithologies and associated textures (from left to write: magmatic (black dots) and crystal plastic fabrics (grey line, running average); Pl and Cpx grain-sizes (mm); 10m running average of number of grain-size contacts) and downhole bulk-rock Mg#. (C) Composition of cores of Cpx crystals (average per sample) in the studied interval from 500 to 800 mbsf; Red diamonds represent coarse-grained Cpx, while blue diamonds display the composition of fine-grained crystals. The grey horizontal bar represents the drilled interval with no recovery (see MacLeod et al., 2017).

6
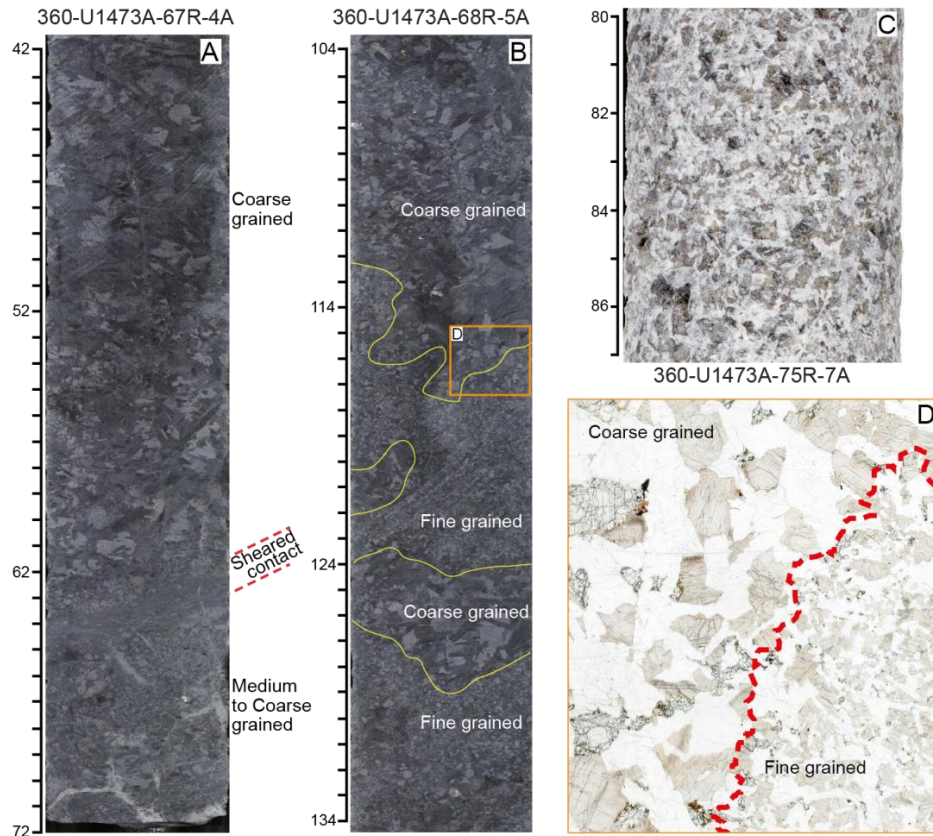
181

182 ***Figure 2***: Examples of grain-size variations in olivine gabbros from Hole U1473A. In (A) the contact between
183 coarse (on top) and medium (bottom) is marked by a shear band were intense grain-size reduction is recorded. (B)
184 Sutured and lobate, irregular grain-size contacts preserve their primary characteristics; orange box locates the thin
185 section reported in (D). (C) Isotropic magmatic fabrics typically observed in the studied samples at the
186 macroscopic scale. (D) Thin section showing the irregular, magmatic contact between coarse- and fine-grained
187 olivine gabbros.

188

189

3. Sampling and petrography

190

191   The samples investigated herein were selected from the olivine gabbros described in
192 Ferrando et al. (in revision, 2021), and sampled from the 500-800 mbsf depth interval in IODP
193 Hole U1473A, where was presented a comprehensive petro-geochemical study of pristine
194 olivine gabbros devoid of crystal-plastic deformation overprint and characterized by primary
195 grain-size variations. Here, we performed petrographic observations and microstructural
196 analyses on 15 selected olivine gabbros (Table 1), all sampled across grain-size contacts.

197

198

199 ***Table 1***: List of samples (R= Rotary core barrel; W=working half) and quantified EBSD grain size parameters for crystals of plagioclase (Pl), clinopyroxene (Cpx) and olivine
200 (Ol). Opx=orthopyroxene; SF=ShapeFactor; MGD=Maximum Grain Deformation (maximum Mis2Mean for each detected grain); GOS=Grain Orientation Spread. Sample
201 names are reported as (360-U1473A-) core-section-interval (in centimeters).
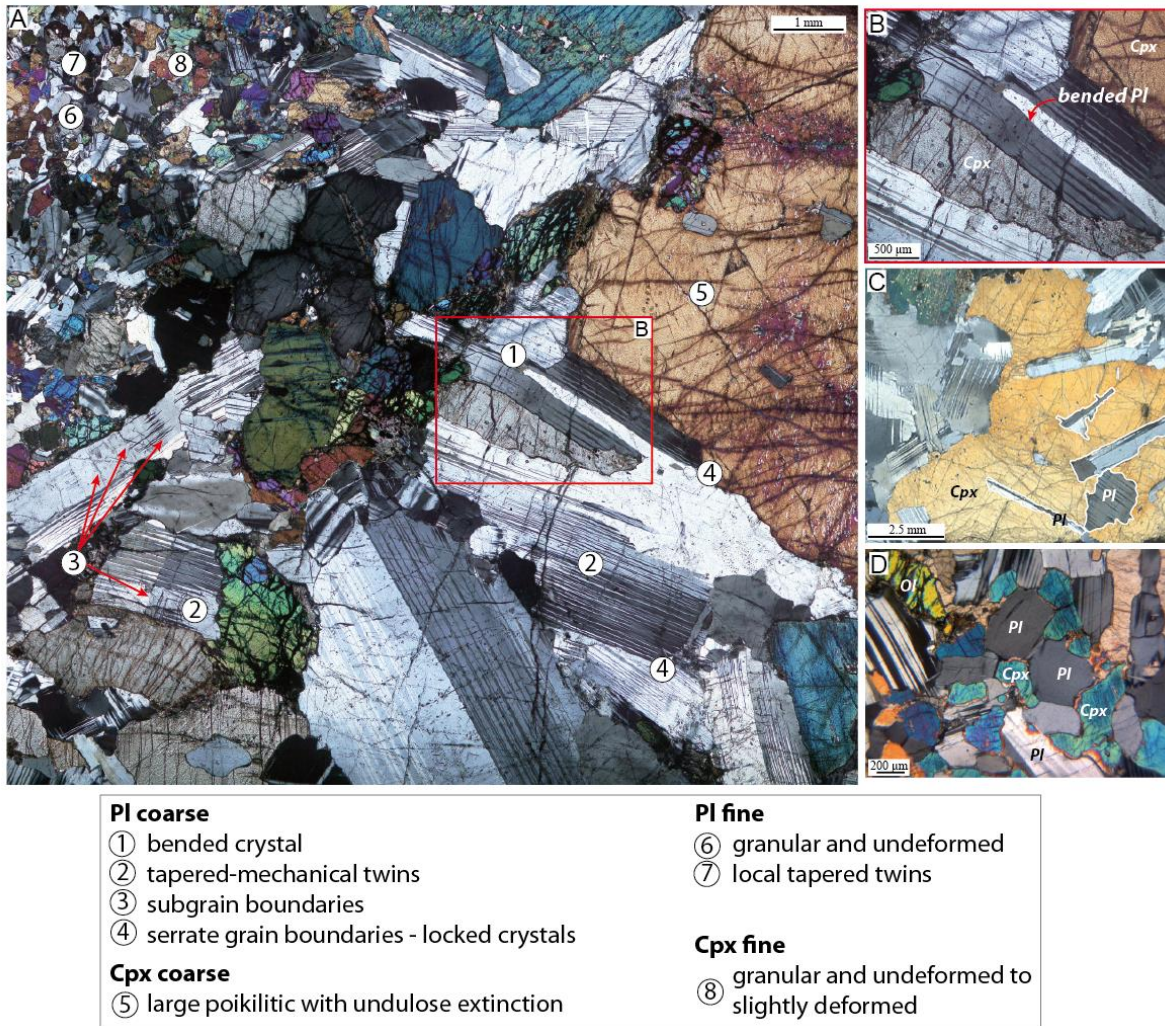
Full sample name	Short name	Mineral modal %				EBSD setup		Fine/ Coarse	Plagioclase Grain analyses					Clinopyroxene Grain analyses				Olivine Grain analyses		
		Ol	Pl	Cpx	Opx	Analyzed area (mm)	Step size		Mean Area	Mean SF	GOS	Mean MGD	Aspect Ratio	Mean Area	Mean SF	GOS	Mean MGD	Mean Area	GOS	Mean MGD
64R-8W, 128-139	64-8	6	54	38	2	33x19	30	Fine	104534	1.59	1.19	4.13	2.77	93064	1.76	1.00	3.35	77700	1.17	3.84
								Coarse	3740589	3.17	2.55	12.98	3.04	4928658	8.47	1.80	11.33	1889859	5.76	20.15
65R-6W, 98-108	65-6	7	56	34	3	29x18	17	Fine	112069	1.78	0.92	4.05	3.10	65044	1.94	0.68	2.75	83215	1.10	3.98
								Coarse	2515828	3.69	1.79	11.34	3.47	1854449	7.27	1.60	9.35	3980253	4.10	15.94
67R-3W, 73-77	67-3	5	63	31	1	35x19	20	Fine	131529	1.77	0.95	4.33	3.48	97922	2.09	0.88	3.37	89241	0.98	3.41
								Coarse	2706661	3.61	1.47	9.9	3.85	3595432	8.6	1.53	9.92	3796765	4.45	17.11
67R-5W, 53-56	67-5	5	56	36	3	28x19	18	Fine	98502	1.71	0.70	2.94	2.99	71785	1.98	0.51	2.03	62097	0.90	3.15
67R-5W, 60-63						26x19	30	Coarse	3103811	2.88	2.04	9.73	3.64	3407677	5.82	1.40	8.49	1550363	2.81	9.00
67R-6W, 4-9	67-6	6	63	29	2	37x18	18	Fine	88534	1.71	0.83	3.61	2.98	101646	2.2	1.02	3.91	113703	1.54	4.71
								Coarse	2607872	4.24	1.66	10.28	2.70	2220167	11.43	2.42	11.33	1551830	2.30	9.84
67R-8W, 4-8	67-8	7	63	28	2	36x18	35	Fine	117620	1.64	1.52	5.05	2.76	86925	1.74	1.09	3.6	104000	1.43	4.36
								Coarse	3222704	2.87	2.26	11.88	3.84	2052652	5.51	2.30	12.29	1539952	2.86	12.13
68R-5W, 64-70	68-5	6	58	35	1	36x20	20	Fine	125481	1.7	0.66	2.89	2.97	114271	2.1	0.67	2.57	93933	0.70	2.60
								Coarse	2793983	3.18	1.54	9.07	3.44	2133945	6.55	0.98	6.37	2699760	2.71	11.55
74R-7W, 106-113	75-7	5	48	46	1	22x19	25	Fine	136288	1.71	1.02	4.01	3.53	112598	2.06	0.91	3.55	107535	1.30	3.98
								Coarse	3025000	3.01	1.70	11.02	3.66	5471934	10.45	1.17	11.91	2518750	2.59	15.91
78R-7W, 68-74a	78-7	8	66	25	1	28x18	30	Fine	121992	1.63	0.73	2.74	3.04	74763	1.74	0.65	2.28	86357	1.18	3.57
								Coarse	4549951	2.76	1.27	8.57	3.46	2872112	7.10	0.80	6.45	1851975	4.44	14.58
79R-8W, 17-21	79-8	6	53	38	3	35x20	20	Fine	120769	1.74	0.64	2.82	3.10	92912	2.06	0.67	2.79	85917	1.32	4.07
80R-4W, 143-146	80-4	13	60	24	3	29x19	30	Fine	131513	1.68	0.48	2.03	3.40	131316	1.98	0.64	2.22	135532	0.71	2.39
								Coarse	2419626	2.83	0.95	6.23	3.27	2638148	6.83	1.12	5.55	1848075	2.24	7.19
80R-8W, 81-87	80-8	12	51	36	1	37x18	20	Fine	149532	1.73	0.78	3.61	3.30	171069	2.26	0.85	3.64	135092	1.04	3.74
								Coarse	3305555	2.96	0.99	8.03	3.55	1880910	5.19	1.13	7.30	1996105	2.05	9.05
83R-4W, 118-124	83-4	5	72	21	2	37x19	20	Fine	114138	1.67	0.51	2.30	2.99	96780	1.91	0.47	2.31	87493	0.79	2.77
								Coarse	6063711	3.68	0.99	6.88	3.17	2057000	8.30	0.85	6.03	2491524	2.84	8.00
89R-6W, 95-99	89-6	22	48	29	1	34x16	30	Fine	149196	1.61	0.77	2.94	3.21	87225	1.82	0.70	2.36	92582	1.33	3.62
								Coarse	5239306	2.85	1.39	8.47	4.45	7608654	9.07	1.40	10.07	14439820	3.61	13.64

202

8

The magmatic, irregular grain-size variations (Fig. 2b) are characterized by sutured grain-size contacts displaying variable orientations (Fig. 2b,d). Olivine gabbros from both coarse-grained and fine-grained intervals contain cumulus assemblages of subhedral to anhedral olivine (Ol), equant euhedral to subhedral and lath-shaped plagioclase (Pl), and granular to poikilitic clinopyroxene (Cpx). Mineral SPO is overall random or very weak resulting mostly in isotropic textures at the macroscopic scale (Shipboard data; MacLeod et al., 2017; Fig. 2c). Coarse-grained domains show variable thickness and are embayed by domains of fine-grained olivine gabbro (Fig. 2b). Textures of coarse-grained olivine gabbro are predominantly subophitic (Fig. 2d), with plagioclase chadacrysts showing lobate contacts against clinopyroxene oikocrysts. Along the grain-size magmatic contacts, coarse-grained minerals are locally truncated (mainly Pl) and commonly display lobate contacts against fine-grained counterparts. These grain-size textural relationships have been interpreted as the result of early formation of the coarse-grained intervals and later emplacement of melts forming the fine-grained olivine gabbros (see Ferrando et al., in revision). The fine-grained intervals display granular textures (Fig. 2d) likely resulting from *in-situ* adcumulus growth.

The subophitic textures of coarse-grained olivine gabbros are characterized by overall randomly oriented Pl crystals (Fig. 3a), subhedral to anhedral Ol and large anhedral (Fig. 3b) to poikilitic Cpx locally embaying Pl chadacrysts (Fig. 3a,c). Coarse Pl crystals have characteristic elongated shapes (Fig. 3a-c). Tapered (mechanical) twins are commonly observed in coarse Pl crystals, especially in contact or nearby Cpx crystals (Fig. 3a). Elongated Pl with the highest aspect ratios (long axis/short axis) are locally bent (Fig. 3a,b) and display subgrain boundaries perpendicular to the crystal elongation direction (Fig. 3a). At the contact with coarse Cpx, these high aspect ratio Pl tend to bend around the Cpx crystals (Fig. 3b). Pl grain boundaries are serrate at contacts with other coarse Pl, resulting in crystal interlocking (Fig. 3a). Coarse Ol crystals show well-developed subgrain boundaries. Large oikocrysts of Cpx show undulose extinction displaying minor subgrain boundaries.

The granular textures of fine-grained olivine gabbros display euhedral to subhedral crystals showing smooth, equilibrated crystal boundaries (Fig. 3a,d). Fine-grained Pl crystals have generally rounded shapes or are slightly elongated with low aspect ratios and show scarce or lacking twins (Fig. 3d). Subgrain boundaries are not developed in fine-grained Ol crystals (Fig. 4e,f). Fine-grained Cpx crystals occur mostly as interstitial grains (Fig. 3a,d) and show undulose extinction in only a few grains, without remarkable subgrain boundaries (Fig. 4g,h).

Pl coarse
1. bended crystal
2. tapered-mechanical twins
3. subgrain boundaries
4. serrate grain boundaries - locked crystals

Cpx coarse
5. large poikilitic with undulose extinction

Pl fine
6. granular and undeformed
7. local tapered twins

Cpx fine
8. granular and undeformed to slightly deformed

Figure 3: Textures of coarse- and fine- grained olivine gabbros. (A) Sample 360-U1473A-66R-7W, 12-18 cm best illustrating the characteristic textures of both coarse- and fine-grained olivine gabbros (numbers indicate the microstructures listed at the bottom of the figure). (B) Close-up showing a bent Pl around nearly-rigid Cpx. (C) Large poikilitic clinopyroxene oikocryst embay plagioclase showing corroded grain boundaries in sample 74 360-U1473A-64R-4W, 19-24 cm. (D) Undeformed fine-grained olivine gabbro with typical granular textures.

4. Methods

Microstructures were analytically characterized on whole thin sections by Electron Backscattered Diffraction (EBSD) technique using the Field Emission Gun CamScan X500FE CrystalProbe facility at Géosciences Montpellier (University of Montpellier). Diffraction patterns were recorded by the Nordlys Nano EBSD CCD Camera, , installed perpendicular to the incident electron beam, with an angular resolution of 0.3°. Operating conditions were a 20 kV accelerating voltage, a 5 nA beam current, and a working distance of 25 mm under low vacuum conditions (2 Pa of gaseous Nitrogen). Areas of ~ 35x20 mm were mapped for each sample at different sampling step sizes ranging between 17 μm to 35 μm depending on the

251 minimum grain size of the analyzed sample (Table 1). EBSD raw data were first processed
252 using the CHANNEL5 software from Oxford Instruments HKL to remove isolated single
253 pixels and to increase the indexation rate by filling automatically the non-indexed pixel having
254 up to 8 indexed neighbors. Indexation rates are ~95% or more. Grain, textural and
255 Crystallographic Preferred Orientation analyses of EBSD data were performed using MTEX
256 4.5.2, an open-source MatLab® toolbox that allows quantitative microstructural analyses
257 covering a wide range of properties (e.g., Hielscher and Schaeben, 2008; Mainprice et al.,
258 2014). Single grains were reconstructed by automatically selecting adjacent pixels having
259 misorientations <10° (misorientation angle >10° mark grain boundaries). Systematic grain
260 identification errors in plagioclase caused by crystal twinning was corrected by automatically
261 merging crystals having misorientation angle >178° between pixels. The mineral modal
262 abundance of each thin section was quantified by EBSD mapping (Table 1).

263

4.1 Grain analyses

265 We performed grain analyses of Pl, Ol and Cpx crystals. The identification of grains
266 using MTEX enables to quantify a series of textural parameters describing the morphology and
267 the intra-crystalline deformation of each detected grain. We determined the number of grains
268 and the area of each grain (in μm^2) by multiplying the number of pixels in the considered grain
269 by the area of one pixel (depending on the analytical step-size). Based on thin section
270 observations, the diameter of fine-grained crystals ranges from <0.1 mm to ~0.8 mm and
271 averages out to ~0.4-0.5 mm (MacLeod et al., 2017; Ferrando et al., in revision), hence we set
272 a threshold of ~10^6 μm^2 grain area to distinguish the fine-grained (<10^6) from coarse-grained
273 (>10^6) crystals.

274 To quantify the tortuosity of the grain perimeter (i.e., morphology), we used the shape
275 factor (Mainprice et al., 2014), which corresponds to the ratio between the perimeter of a grain
276 and its equivalent perimeter (perimeter of a circle that has the same area as the considered
277 grain). High values of shape factor indicate anhedral crystals, as for example interstitial or
278 poikilitic, while low values are typical of granular textures.

279 Intra-crystalline deformation is described by the Mis2Mean parameter that quantifies the
280 misorientation of each pixel within a single grain with respect to the mean orientation of the
281 grain (Mainprice et al., 2014). We determined the average Mis2Mean for each detected grain,
282 hereafter referred to as 'Grain Orientation Spread (GOS)'. Because GOS is the average

misorientation of all pixels in a single grain, the misorientation of just a few pixels is over-weighted in fine-grained crystals and under-weighted in coarse crystals; therefore, the misorientation can be overestimated for fine-grained crystals and underestimated for coarse crystals. To overcome this analytical bias, we also computed the maximum Mis2Mean for each detected grain ('Maximum Grain Deformation', MGD).

Grain area, Shape factor, GOS and MGD of Pl, Ol and Cpx crystals are reported in Table 1.

4.2 Crystallographic Preferred Orientation

To measure representative Crystallographic Preferred Orientation (CPO) of mineral phases, a statistically significant number of grains is needed (arbitrarily set to 100 grains in Satsukawa et al., 2013). In olivine gabbros, this requirement is mostly satisfied by Pl (see mineral grain number in Table 2). For each sample presenting a grain-size contact, two subsets were selected in MTEX, one of coarse- and one of fine-grained interval, to evaluate the fabric characteristics of coarse-grained and fine-grained Pl separately. CPO are presented in equal-area, lower hemisphere stereographic projections (pole figures).

Table 2: Strength of fabrics and Pl CPO parameters. The pf*J*-index is the strength of single pole figures (Mainprice et al., 2014). Short name as in Table 1.

Short name	Fine/ Coarse	n° grains	M-index	J-index	pfJ			BA	L#	F#	K-factor	
					[100]	(010)	(001)		e1/e2 [100]	e1/e2 (010)	[100]	(010)
64-8	Fine	1467	0.032	4.33	1.20	1.22	1.24	0.42	1.31	1.42	1.83	3.54
65-6	Fine	1515	0.042	3.26	1.21	1.22	1.15	0.29	1.13	1.51	0.24	1.87
67-3	Fine	1129	0.021	3.35	1.17	1.33	1.13	0.51	1.21	1.34	0.83	0.69
67-6	Fine	2285	0.038	2.86	1.26	1.25	1.09	0.58	1.43	1.26	0.96	0.45
67-8	Fine	1472	0.040	3.03	1.27	1.34	1.08	0.29	1.16	1.60	0.27	1.90
68-5	Fine	1333	0.019	2.94	1.19	1.17	1.12	0.72	1.37	1.06	1.85	0.17
	Coarse	83	0.035	6.13	1.33	1.57	1.28	0.44	1.15	1.43	0.52	0.74
79-8	Fine	1893	0.030	2.33	1.21	1.21	1.05	0.65	1.47	1.20	1.37	0.35
80-4	Fine	1003	0.034	3.47	1.24	1.19	1.17	0.39	1.32	1.34	0.83	2.20
	Coarse	78	0.044	10.85	1.60	1.73	1.6	0.49	1.34	1.33	0.52	0.62
80-8	Fine	684	0.010	4.37	1.20	1.28	1.16	0.61	1.31	1.24	3.14	1.23
83-4	Fine	1197	0.039	3.1	1.37	1.22	1.14	0.73	1.79	1.14	2.16	0.29
67-5	Fine	2203	0.065	2.65	1.29	1.32	1.03	0.38	1.40	1.69	0.65	1.72
78-7	Fine	1002	0.040	3.57	1.28	1.16	1.18	0.47	1.43	1.33	1.24	1.75

303   Pole figure representations of Pl CPO were calculated using MTEX. The fabric strength

304   of CPO was determined by the *J*-index of the orientation distribution function (ODF; e.g.,

305   Bunge, 1982; Mainprice and Silver, 1993). Because the *J*-index becomes unrealistically high

306   for aggregates <~1000 grains (e.g., Skemer et al., 2005; Satsukawa et al., 2013), we also

307   calculated the M-index that is less dependent on the number of grains (Skemer et al., 2005).

308   The M-index will be here used preferentially for coarse-grained intervals with ~100 grains

309   analyzed. The *J*-index has a value between 1 for a random distribution (isotropic fabrics) and

310   infinity for single crystal orientation, whereas M-index varies from 0 for isotropic fabrics, to

311   1.

312   The CPO pole figure symmetry can be quantified using the eigenvalues ($e_1 \geq e_2 \geq e_3$, with

313    $e_1 + e_2 + e_3 = 1$) of the normalized orientation tensor for each principal crystallographic axis or

314   poles to planes (Mainprice et al., 2014 and references therein). The eigenvalues were here used

315   to evaluate whether the orientation distribution of each crystallographic axis is random or

316   shows point (or cluster) to girdle concentrations. We focused on the Pl [100] axis because it

317   best defines the sample lineation, and the Pl (010) plane that is systematically oriented parallel

318   to the magmatic foliation (e.g., c. The Pl (010) planes thus best describe the foliation even in

319   samples where its observation at the thin section scale is not obvious. On this basis, we

320   computed the BA-index, representative of the CPO symmetry of the Pl [100] and (010)

321   (Satsukawa et al., 2013; Mainprice et al., 2014); the BA-index value is 0 when the (010) pole

322   figure is a perfect point maximum and the [100] pole figure is a perfect great circle girdle

323   (axial-B pattern; Satsukawa et al., 2013), and it is 1 when [100] is a perfect point maxima and

324   (010) shows girdle distribution. Intermediate values of BA-index (~0.5) are defined by point

325   maxima of both [100] and (010) pole figures (P-type pattern; Satsukawa et al., 2013). We also

326   calculated the K-factor as determined by Woodcock (1977) to quantify the orientation

327   distribution of single pole figures (girdles for $0 \leq K < 1$ and clusters for $1 < K \leq \infty$); the K-

328   factor was determined for Pl [100] in order to quantify the strength of lineation in coarse- and

329   fine-grained intervals of the studied samples. Additionally, we calculated the ratio of the

330   maximum to intermediate eigenvalues of [100] and (010) to determine the strength of lineation

331   (L# = $e_{1[100]}/ e_{2[100]}$) and foliation (F# = $e_{1(010)}/ e_{2(010)}$), respectively (following Yaouancq and

332   Macleod, 2000 and Cheadle and Gee, 2017). The latter allowed us to best compare our data

333   with published Pl CPO from other geological settings (i.e., slow-spreading and fast-spreading

334   oceanic crust, and continental layered mafic intrusions; e.g., Cheadle and Gee, 2017).

335   Indices of Pl fabric strength (i.e., *J*, M and pf*J*) and Pl CPO symmetry (i.e., BA-index,

336   K-factor, L# an F#), together with the number of grains detected, are reported in Table 2.

337

5. Microstructures of olivine gabbros

5.1 Quantitative microstructural description

340   Mineral modal abundances are homogeneous in coarse- and fine-grained intervals of a

341   single sample, whereas they slightly vary between samples from different depths (Table 1, Fig.

342   4a,b). In contrast, the morphology and intra-crystalline microstructures of coarse-grained

343   crystals differ systematically from those of fine-grained crystals in all samples (see also

344   *Sampling and Petrography*).

345   Elongated, coarse Pl crystals have lobate and serrate grain boundaries resulting in high

346   values of shape factor, whereas fine-grained granular Pl crystals show low shape factors,

347   consistent with smooth grain boundaries (Fig. 5a: example of shape factor variations in a single

348   sample). Similarly, the poikilitic habit of coarse Cpx crystals is illustrated by higher shape

349   factor compared to granular fine-grained Cpx crystals (Fig. 5b). On average (per sample), shape

350   factors of coarse-grained Pl and Cpx range from 2 to 5 and 5 to 11.5, respectively, whereas

351   shape factors of all fine-grained crystals are ~2 (Fig. 5c).

352   In Figure 4 (c-h) we report EBSD maps of intra-crystalline misorientation (Mis2Mean)

353   for two representative samples and in Figure 5 (d-i) GOS and MGD are provided for individual

354   grains in a single sample and as average values for all samples.

355   EBSD data reveal the occurrence of two types of coarse Pl crystals: *(i)* elongated crystals

356   (long dimension in the [100] crystallographic direction) with high aspect ratios and displaying

357   well-developed subgrain boundaries (Fig. 4c, 6a,c); *(ii)* subhedral crystals with lower aspect

358   ratio and irregular grain boundaries, and showing zonation of intra-crystalline misorientation

359   determined by higher Mis2Mean at the crystal rim compared to the relative core (Fig. 4d). To

360   further quantify the misorientation in single grains, we selected misorientation profiles parallel

361   to the long dimension of Pl (Fig. 6a-d). Profiles of misorientation angles to the orientation of

362   the pixel at distance 0 mm (beginning of the profile: point a, c, c' in Fig. 6a,c) in coarse Pl

363   crystals reveal that bell-shaped profile portions are separated by 'jumps' (sharp increase or

364   decrease) in misorientation angle (blue profile in Fig. 6b,d). The latter correspond to peaks in

365   the misorientation profiles with respect to the neighboring pixel (red profile in Fig. Fig. 6b,d).

366   These jumps and peaks correspond to subgrain boundaries that develop perpendicular to the

long direction of the Pl crystal (Fig. 6a,c), whereas bell-shaped profiles correspond to bent portions of the Pl crystal. Conversely, most fine-grained Pl crystals have homogeneous Mis2Mean and no subgrain boundaries (Fig. 4c,d, 6a), except for a few grains showing intra-crystalline variations in Mis2Mean values. Consistently, flat misorientation profiles are documented in most fine-grained Pl crystals (Fig. 6b).

Coarse Ol crystals display well-developed subgrain boundaries (Fig. 4e,f). The latter are subparallel to each other and are highlighted by jumps and peaks in misorientation profiles (Fig. 6e,f), similarly to those described in coarse-grained elongated Pl crystals. Fine-grained Ol crystals show homogeneous and low Mis2Mean (Fig. 4e,f).

Coarse Cpx crystals display rather low Mis2Mean, although some grains show higher Mis2Mean values (Fig. 4g,h). Fine-grained Cpx crystals also show overall low Mis2Mean, but locally they display higher Mis2Mean (Fig. 4g,h).

Overall, the EBSD microstructural data indicate that coarse-grained crystals show evidence of intra-crystalline deformation whereas the fine-grained crystals are mostly plastically undeformed. This tendency is quantified by a general smooth increase of GOS with increasing grain area in each sample (Fig. 5d-f). Although this tendency is ubiquitous in all samples (Fig. 5f), variations of GOS in Pl and Cpx in a single sample are scattered for GOS > 2° (Fig. 5d-f). The within-sample trends of MGD also display a positive correlation with grain area (Fig. 5g-i). Notably, the curve of MGD variations (Fig. 5g,h) is steeper in the range of grain area of fine crystals, and then flattens around a value of 10° when the grain size of coarse crystals is reached.
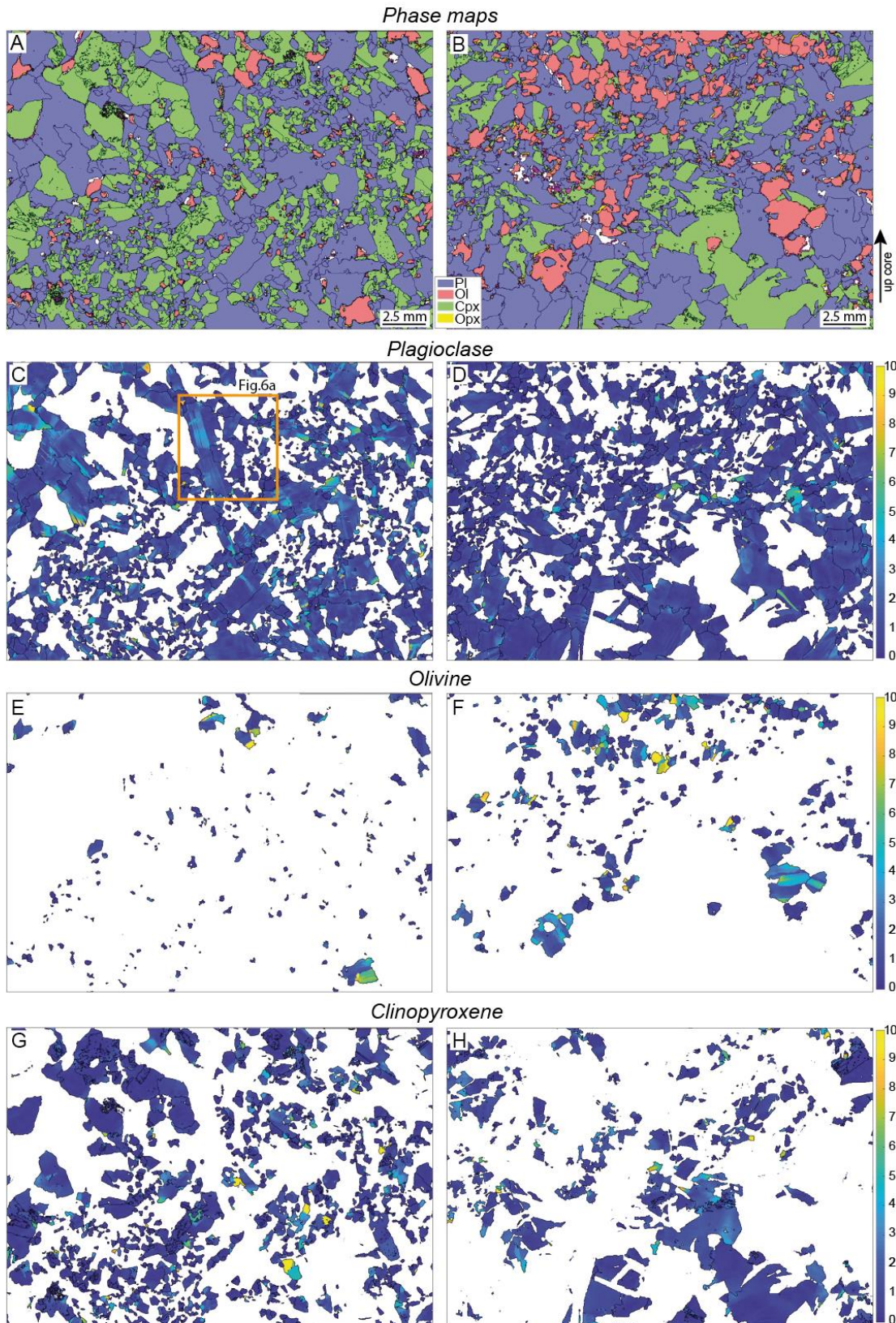
Figure 4: Phase maps (A-B) and Mis2Mean maps (C-H) obtained by Electron Backscattered Diffraction analyses. We report the examples of two representative samples: (A, C, E, G) are maps of sample 360-U1473A-68R-5W, 64-70 cm and (B, D, F, H) of sample 360-U1473A-80R-4W, 143-146 cm. Color coding is reported in the legend and the scale of Mis2Mean on the right. Mis2Mean maps of Pl, Ol and Cpx are shown in (C-D), (E-F) and (G-H), respectively.
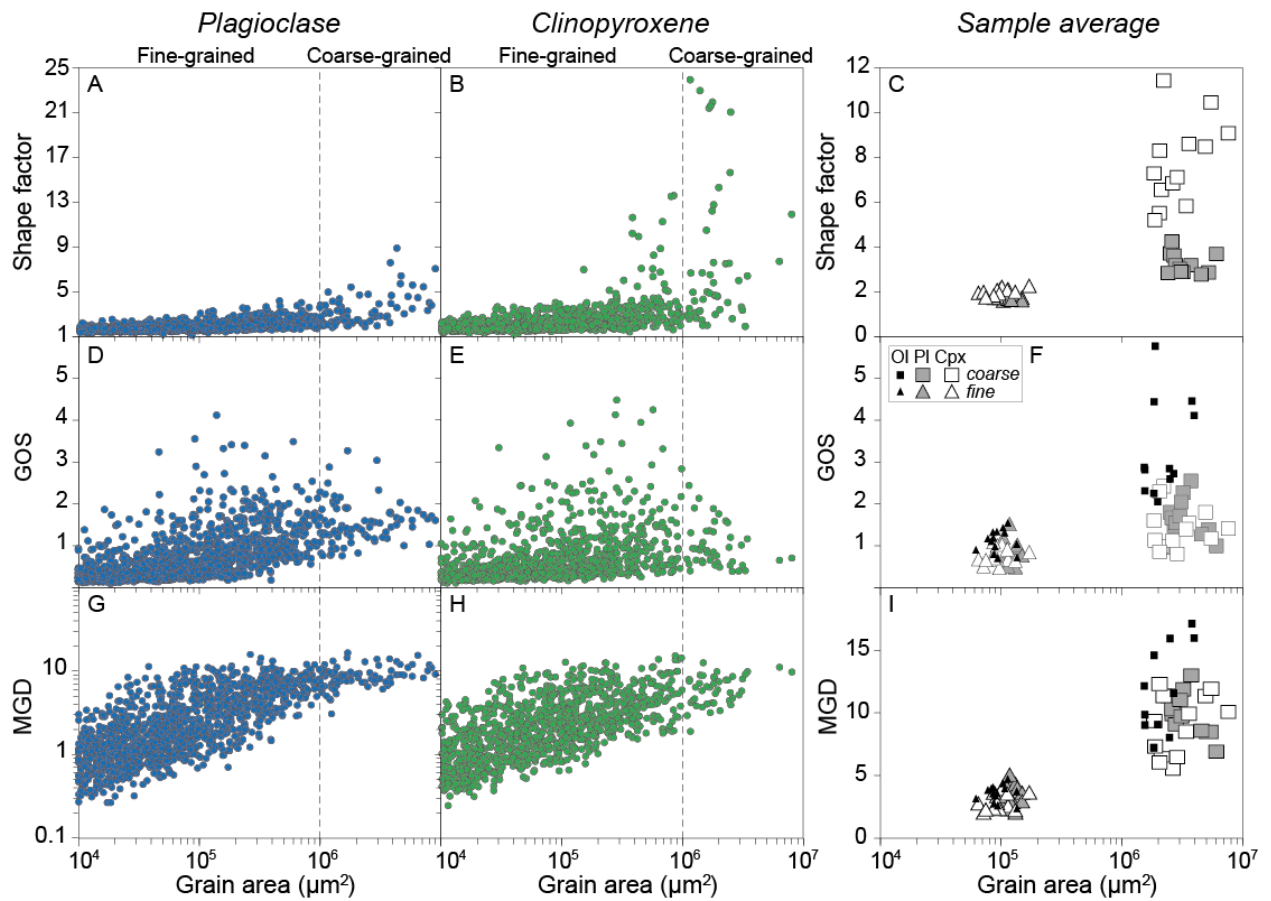
Figure 5: Shape factor and misorientation parameters, i.e. Grain Orientation Spread (GOS) and Maximum Grain Deformation (MGD), of Pl (A, G, D) and Cpx (B, E, H) in sample 360-U1473A-68R-5W, 64-70 cm (see relative EBSD maps in Fig. 4), and all averages per sample for Ol, Pl and Cpx (C, F, I). In C, F, I the grain area is the average grain area per sample. Variations of the parameters are similar in all studied samples, although here we report the details for only one representative sample. All parameters were obtained by grain analyses of the EBSD data (see main text for further details). A threshold of grain area of 10^6 μm^2 was set to distinguish fine-grained ($<10^6$ μm^2) from the coarse-grained counterparts.
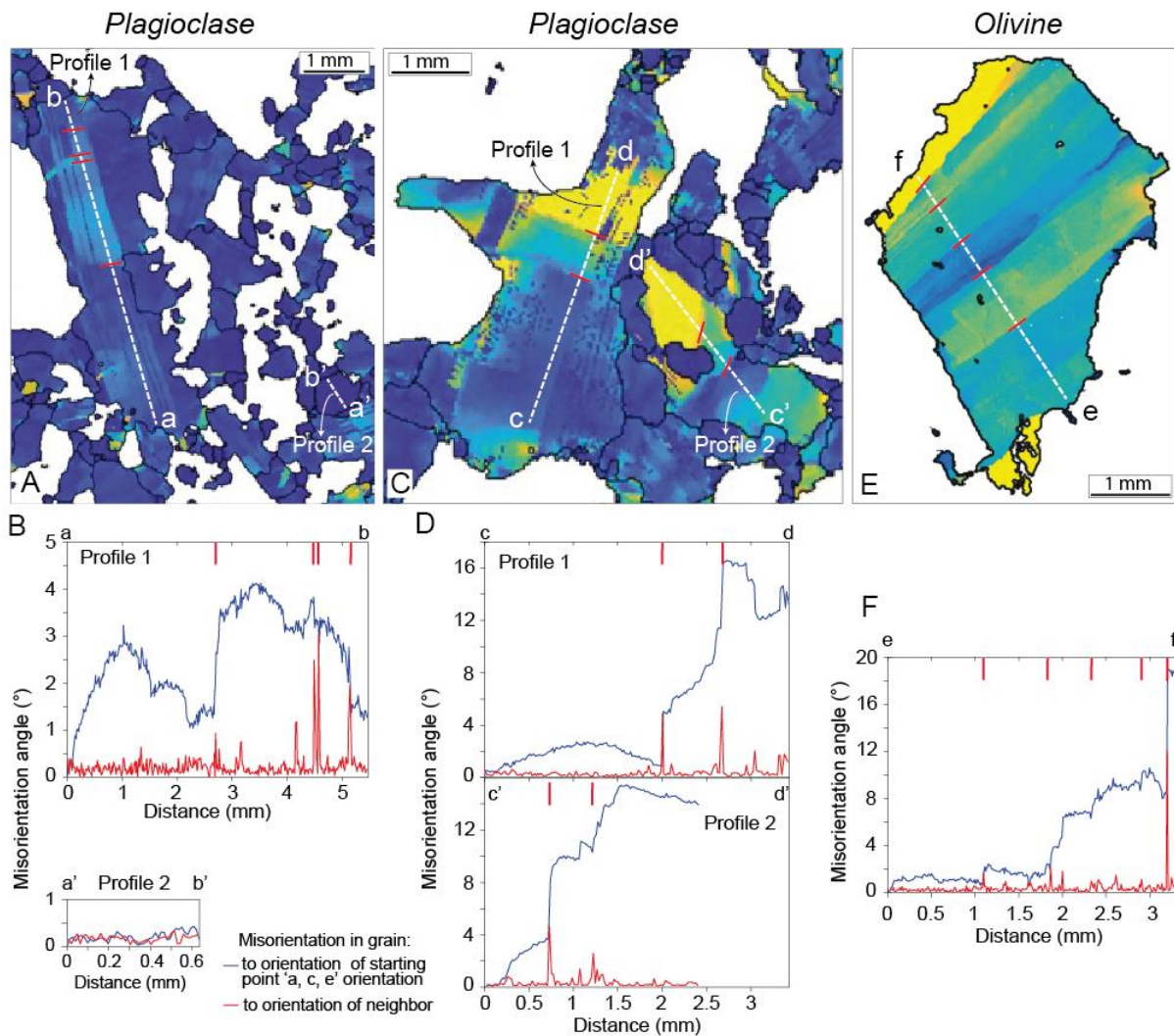
Figure 6: Two examples of deformed coarse-grained Pl associated with undeformed fine-grained Pl (A, C) and deformed coarse-grained Ol (E) in Mis2Mean EBSD maps; the color scale is the same as that reported in Fig. 4). White dashed lines trace the misorientation profiles reported in B, D and F. The red tick-marks highlight the occurrence of subgrain boundaries, which are absent in undeformed grains. Two types of misorientation profiles are presented: the misorientation of each pixel along the profile is measured to the orientation of the pixel at the starting point (i.e., 0 mm; a, a', c, c', e; blue profile), and to the orientation of the neighboring pixel (red profile).

5.2 Plagioclase CPO

More than 1000 Pl grains were measured in fine-grained olivine gabbro, allowing us to obtain reliable CPO. A series of representative Pl CPO is reported in Figure 7. All CPO of coarse-grained intervals were computed in aggregates <100 grains; we show the two CPO with the highest number of measured grains. Because *J*-index is overestimated for these coarse-grained intervals (e.g., Satsukawa et al., 2013; Mainprice et al., 2014), we preferentially use the M-index to quantify the fabric strength.

The fabric strength of the studied samples is dominantly weak and characterized by low *J*- and M-indices (Fig. 7, 8 and Table 2). These fabrics are similar to those typical of magmatic origin in oceanic crustal systems, and overall fall within the lowest values of compiled *J*-index of samples from different geological settings (comprehensive database of Pl CPO from Satsukawa et al., 2013). In particular, the observed weak fabric strengths are comparable with magmatic fabrics documented in gabbros from slow-spreading oceanic crust (Fig. 8), which are generally lower than fabrics of samples from fast-spreading oceanic crust (see also Satsukawa et al., 2013). Although Pl CPO are characterized by low fabric strength (Table 2 and Fig. 8), clear patterns of orientation distribution are observed. Overall, all measured Pl CPO range between axial-B and type-P patterns (from Satsukawa et al., 2013; Fig. 7).

Fine-grained intervals are dominantly characterized by girdle distribution of [100] perpendicular to point maxima of (010), and weak to random orientations of (001). Commonly, the [100] girdle distribution display a point maxima (Fig. 7). Some samples (i.e., 67R-6W, 4-9; 68R-5W, 64-70; 79R-8W, 17-21; 83R-4W, 118-124) show stronger point distribution of [100] and tend to have girdle distribution of (010) with point maxima (Fig. 7). The variable Pl CPO symmetry is quantified by variable BA-indices and [100] K-factor (Fig. 8). Samples with girdle distribution of [100] and (010) point maxima have low BA-index (0.15-0.4) and low K-factor (<1), while samples with [100] point maxima (or cluster distribution of [100]; see Fig. 8) and (010) tending to a girdle-like distribution have higher BA-index (up to 0.75) and high K-factor (>1). Consistently, the strength of magmatic lineation L# is variable, showing the highest values in samples displaying point maxima of [100]. The strength of magmatic foliation F# is low, ranging between 1 and 1.7 (Figs. 7, 9).

CPO of coarse-grained intervals are mostly random. They show low to intermediate BA-indices and rather low K-factor (<1.5) (Fig. 7, 8), L# and F# (Figs. 7, 9).
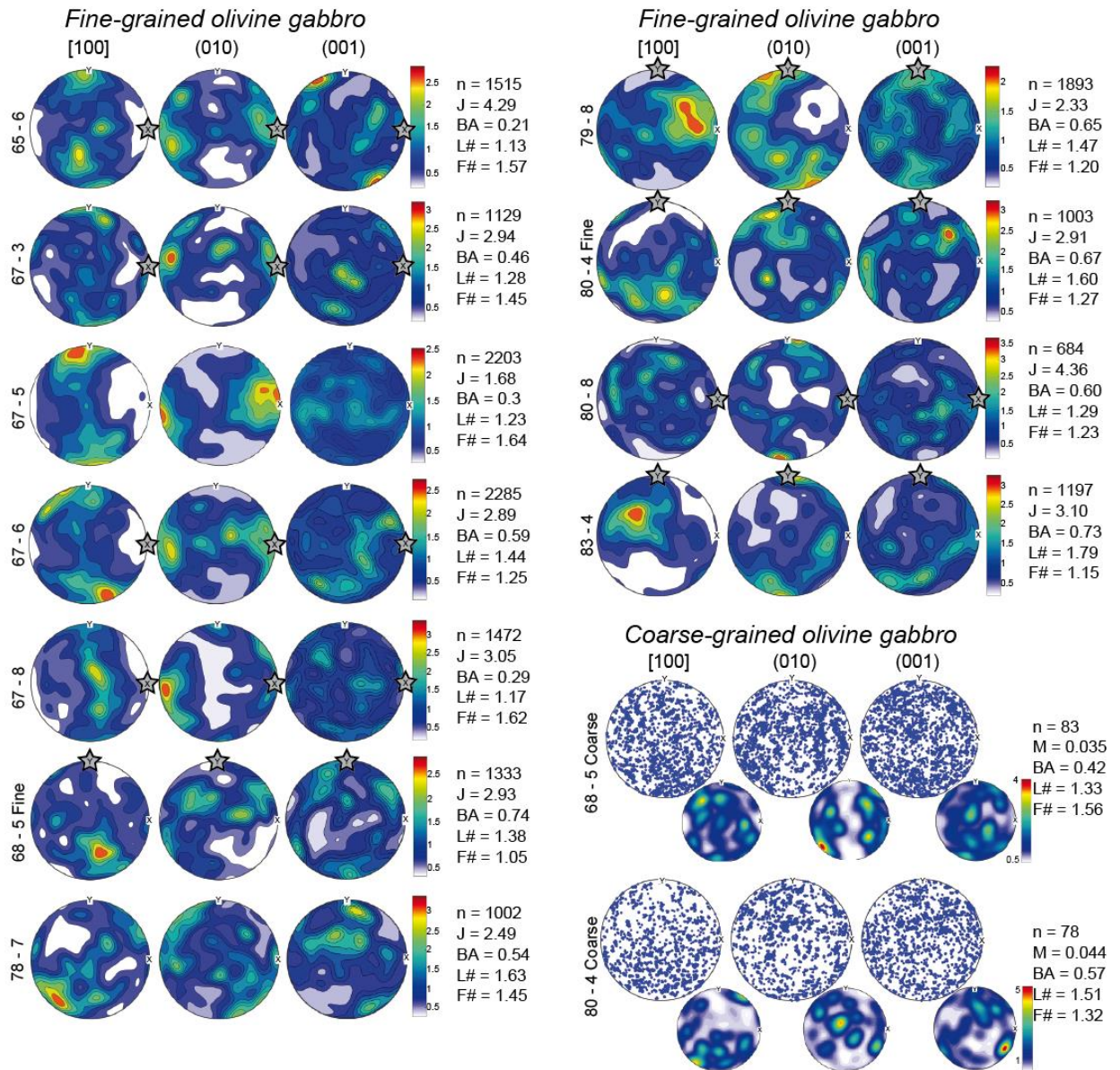
Figure 7: Pl crystallographic preferred orientations (CPO) in olivine gabbros from IODP Hole U1473A. CPO are equal- area, lower hemisphere stereographic projections of all measured pixels; projections are reported in the core reference frame. Pl CPO in fine-grained olivine gabbros are distribution plots; due to the low number of analyzed grains, for coarse-grained olivine gabbros we report scattered plots. Sample names are located on the left of each CPO in the form (360-U1473A-)XX(R)-Y(W) where XX and Y are the section and core numbers, respectively. The stars indicate the vertical of the drill core.

454
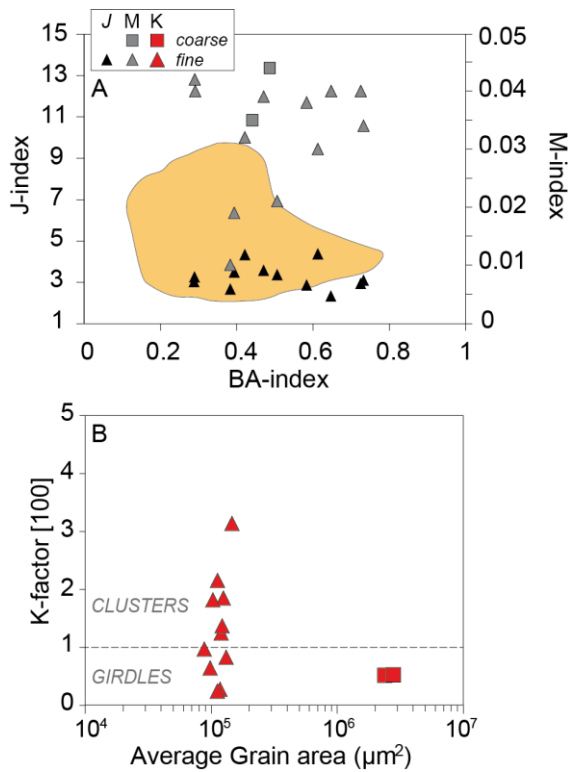
Figure 8: Indices of Pl fabrics. (A) BA-index vs *J*- and M- indices of the studied fine- (triangles) and coarse-grained (squares) olivine gabbros; the *J*-index of magmatic fabrics developed at slow-spreading environments from the database by Satsukawa et al. (2013) are also reported for comparison (orange field). (B) Average grain area vs K-factor of [100]-axis only; a girdle distribution is considered with K-factor<1, while cluster distribution refers to K-factors>1.

6. Discussion

6.1 Magmatic fabrics as indicative of the geological context

The development and strength of magmatic fabrics in gabbroic rocks vary according to the geodynamic context of formation (e.g., Satsukawa et al., 2013; Cheadle and Gee, 2017). Pl is the most abundant mineral phase constituting gabbroic rocks, and its fabric records the high temperature processes that occurred prior to cooling of the mafic intrusions. Accordingly, Pl fabrics have been widely used to understand the emplacement of crystal mushes in continental (e.g., Higgins, 1991, 2006; Meurer and Boudreau, 1998; Ji et al., 2014; Bertolett et al., 2019) and oceanic crust or ophiolite analogues (e.g., Nicolas and Ildefonse, 1996; Nicolas et al., 2009; Morales et al 2011; Satsukawa et al., 2013; VanTongeren et al., 2015; Brown et al., 2019); fundamental differences in Pl fabrics were delineated among these geological contexts (Satsukawa et al., 2013; Cheadle and Gee, 2017). While the BA-index describes the Pl CPO symmetry and provides a single quantification of both foliation and lineation strengths

(Mainprice, 2014), Cheadle and Gee (2017) proposed that specific correlations between magmatic foliation (F#) and lineation (L#) are indicative of the context of formation of gabbroic rocks (Fig. 9a). Overall, fabrics of Pl from Layered Mafic Intrusions (LMI) (e.g., Higgins, 2006; Holness et al., 2017; Bertolett et al., 2019) are characterized by medium to strong foliations (high F#) and weak lineations (low L#), Pl fabrics from fast-spreading ridges are typically characterized by relatively strong foliations and lineations (medium to high F# and L#) (e.g., MacLeod et al., 1996; Nicolas et al., 2009; Morales et al., 2011; VanTongeren et al., 2015; Brown et al., 2019), and Pl fabrics at slow-spreading ridges show weak foliations (low F#) and variable lineation intensity (low to high L#) (e.g., Satsukawa et al., 2013; Cheadle and Gee, 2017). The strength of these F# and L# structural parameters can be related to physical processes occurring in each geological environment during the formation of the gabbroic bodies, and can be summarized as follows:

1) In LMI, the typically described large magma bodies over 1 kilometer in thickness (e.g., Cashman et al., 2017; Fig. 9b) are filled by long-lived and static crystal mushes (e.g., Bédard, 2015). These large magma reservoirs contain a significant amount of melt (and thus porous space) that allow settling of the crystallizing minerals, in principle without any further perturbation. Crystal settling leads to the development of foliations (e.g., Wager and Brown, 1968; Holness et al., 2012; Ji et al., 2014), while lineations are rare (e.g., Higgins, 2006). Moreover, density-controlled settling can drive crystal segregation during fractional crystallization, leading to the formation of monomineralic layers (e.g., Wager and Brown, 1968; Higgins, 1991). In addition to the settling process, the strength of foliations in LMI also results from compaction of the crystal mushes. Indeed, continental magmatic systems are composed of multiple crystal mushes distributed throughout the lower crust (Fig. 9b), which can locally be as small as ~150m-thick (e.g., Holness et al., 2017). The weight of the uppermost denser crystal mushes can drive compaction of the deeper magma chambers, thus reducing the amount of interstitial melt and resulting in the development of stronger foliations (high F#, Fig. 9a; e.g., Holness et al., 2017; Bertolett et al., 2019).

2) At fast-spreading ridges or in fast-spreading ophiolite analogues, the oceanic crust is formed in non-static crystal mushes and a shallow Axial Melt Lens (AML) (Fig. 9c). There, fabrics of oceanic gabbros are strongly controlled by the fast spreading rates that are accommodated by magmatic accretion (e.g., Boudier et al., 1996; Kelemen and Aharanov, 1998) and continuous lateral flow along the spreading direction (e.g., Nicolas et al., 2009; Fig. 9c). The development of strong foliations (high F#) in those gabbros may result from *(i)*

508   compaction of the crystal pile (e.g., VanTongeren et al., 2015), *(ii)* subsidence along the magma

509   chamber walls prior to its horizontal movement away from the AML (e.g. Nicolas et al., 2009;

510   Brown et al., 2019), and/or *(iii)* upward migration of interstitial melts through a magma mush

511   column, from the lower gabbros to the AML (e.g., Yaouancq and Macleod, 2000; Mock et al.,

512   2020). Additionally, these foliated gabbros often present weak to medium lineations resulting

513   from crystal alignment during the spreading-related lateral flow of the oceanic lithosphere.

514   *3)* The ultraslow- to slow-spreading oceanic crust is built up by ephemeral small

515   magmatic bodies, as evidenced by the absence of quasi-permanent magma lenses (e.g., Sinton

516   and Detrick, 1992; Canales et al., 2017; Fig. 9d). Slow spreading is accommodated by extensive

517   faulting during discontinuous melt supply (e.g. Cannat et al., 2006; Escartín et al., 2008;

518   MacLeod et al., 2009; Blackman et al., 2011). The cooling rates estimated for gabbroic

519   sequences sampled at Atlantis Massif OCC (MAR, Schoolmeesters et al., 2012; Ferrando et

520   al., 2020) and Atlantis Bank OCC (John et al., 2004; Coogan et al., 2007) indicate that those

521   magma bodies cool rather rapidly. The small dimension of magma bodies at slow-spreading

522   ridges, together with their ephemeral character and fast cooling, likely preclude extensive

523   crystal settling and alignment, in turn preventing the development of strong magmatic

524   foliations and, as a consequence, low F# (Satsukawa et al., 2013; Cheadle and Gee, 2017).

525   Along slow- to ultraslow-spreading ridges, the formation of the oceanic crust at OCCs

526   involves a complex history of discontinuous magmatism and magma emplacement in a

527   continuously uplifted and deforming lower oceanic crust. Consequently, extensive crystal-

528   plastic deformation is commonly recorded in the upper sections of exposed oceanic crust, and

529   in the vicinity of the detachment fault. There, foliations and lineations developed during plastic

530   deformation are able to overprint all primary fabrics (e.g., Allard et al., 2020). An example is

531   shown in Figure 2a, where a sheared grain-size contact likely developed at the expenses of a

532   pre-existing primary contact. Crystal-plastic deformation and shearing at OCCs are considered

533   to be related to the development and continuous activity of the detachment fault (e.g., Miranda

534   and John, 2010; MacLeod et al., 2017; Dick et al., 2019a). This widespread crystal-plastic

535   deformation overprint hampered the documentation of the magmatic fabrics characterizing the

536   slow-spread gabbroic crust, nowadays still poorly constrained. Although IODP Hole U1473A

537   shows widespread crystal-plastic deformation, it decreases in the deepest 200 m of the hole,

538   where it is locally absent (Fig. 1) and primary magmatic features are still present. We

539   emphasize that our sampling strategy focuses on samples that lack evidence of crystal-plastic

540   deformation; accordingly, neoblasts of recrystallized primary mineral phases are nearly absent

541 in all selected olivine gabbros and grain-size reduction related to dynamic recrystallization is
542 not observed. Also, the irregular and locally lobate shape of the studied grain-size contacts
543 cannot result from plastic deformation, which would lead to straight contacts (Fig. 2a).

544   The magmatic fabrics documented in the studied olivine gabbros are consistent with BA
545 index, as well as L# and F# values reported in slow- to ultraslow-spreading oceanic crust
546 (Satsukawa et al., 2013. Cheadle and Gee, 2017), thus confirming that these geological
547 environments are characterized by weak foliations (low F#) and variable lineations (low to high
548 L#) (Fig. 9a). In the following sections, we better constrain the processes driving the
549 development of Pl magmatic fabrics in a section of ultraslow-spreading lower oceanic crust.

550
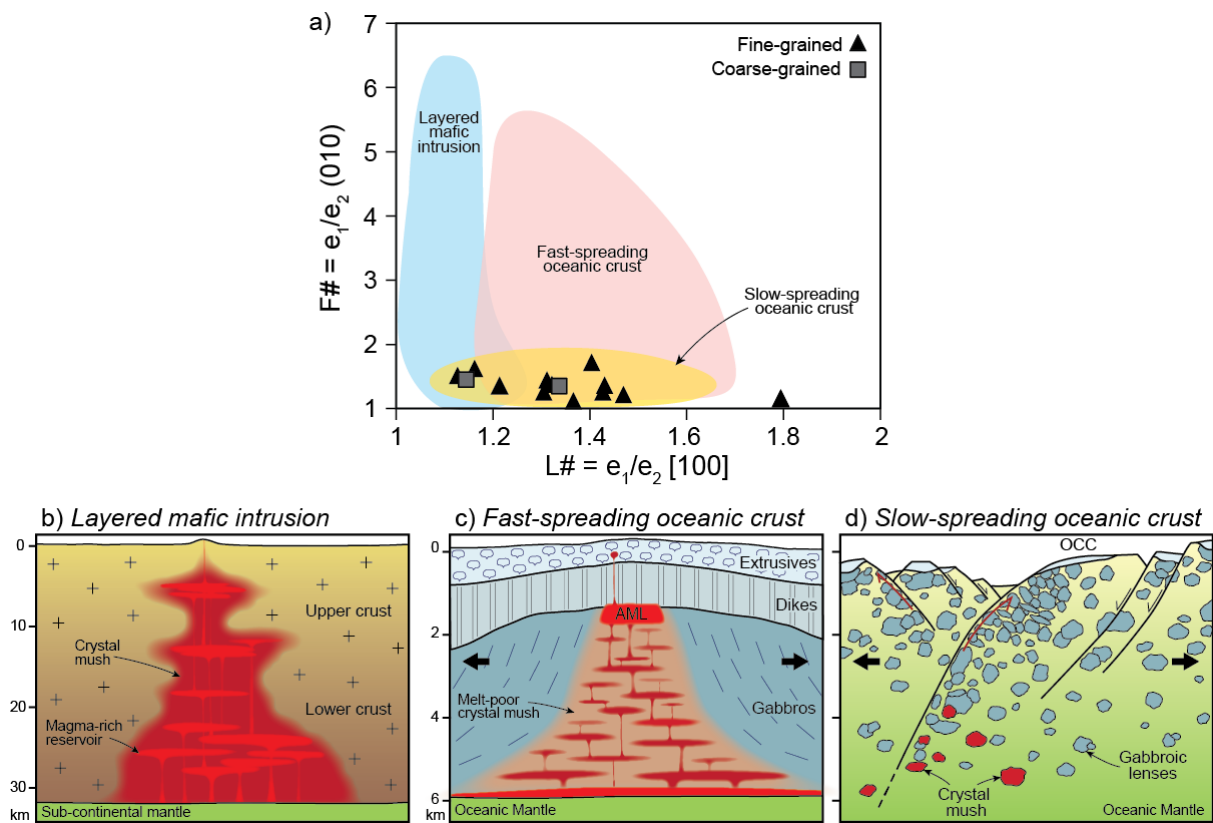
551

552 **Figure 9**: (A) Strength of lineation (L#) and foliation (F#) in gabbros from layered mafic intrusions (blue field),
553 fast-spreading (pink field) and slow-spreading oceanic crust (yellow field) modified after Cheadle and Gee (2017).
554 Results from this study are reported distinguishing fine-grained (triangles) and coarse-grained (squared) olivine
555 gabbros. The bottom of the figure shows sketches of the plumbing system architecture at the three different
556 geological environments: (B) large crystal-mush reservoirs build continental layered mafic intrusion (modified
557 after Cashman et al., 2017); (C) rather large crystal mush zone forms the lower oceanic crust providing magma to
558 the static Axial Melt Lens (AML) below fast-spreading ridges (modified after France et al., 2009); (D) Small and
559 ephemeral crystal mushes cooling to form gabbroic sequences in the lower oceanic crust at slow-spreading ridges.

560

561

6.2 Microstructural features of magmatic deformation at Hole U1473A

6.2.1 Intra-crystalline deformation: coarse- vs fine-grained intervals

Coarse-grained Ol crystals are characterized by well-developed subparallel subgrain boundaries highlighted in Mis2Mean EBSD maps (Figs. 4e-f) and misorientation profiles (Fig. 6e-f). Their average GOS and MGD are rather high and plot above values obtained for fine-grained Ol crystals (Fig. 5f,i). Coarse-grained Pl crystals commonly display mechanical twins (Fig. 3a) and subparallel subgrain boundaries perpendicular to their elongation direction (Fig. 3a, Fig. 6a-d). Pl crystals with high aspect ratio are often bent against Cpx crystals (Fig. 3a,b). When Pl crystals are interlocked, their contacts are locally lobate (Fig. 3a), as illustrated by relatively high shape factors (i.e., higher than fine-grained Pl; Fig. 5a). At these lobate contacts, deformation at Pl-Pl and Pl-Cpx grain boundaries led to the incipient development of subgrain boundaries and mechanical twins in Pl crystals. On average, coarse-grained Pl crystals have higher GOS and MGD than the fine-grained crystals (Fig. 5f,i). In summary, coarse-grained Pl and Ol are characterized by extensive intra-crystalline deformation. In contrast, coarse-grained Cpx show undulose extinction with a lack of clear microstructural evidence of deformation (i.e., no subgrain boundaries; Fig. 3a); yet, GOS and MGD are higher in coarse-grained Cpx crystals compared to their fine-grained counterparts (Fig. 5e,f,h,i). This suggests that during magmatic processes and high-temperature deformation of the crystal mush, Cpx was the most rigid mineral phase in the crystal mush, as documented in deformation experiments (e.g., Dimanov and Dresen, 2005).

Ol subgrain boundaries are indicative of dislocation creep at high temperatures. Applying experimental flow laws to partially molten gabbro, Yoshinobu and Hirth (2002) showed that Ol is the weakest phase compared to Pl and Cpx at hypersolidus conditions. Plastic deformation of Ol in the studied coarse-grained olivine gabbros suggest that deformation occurred when the crystal framework was already interlocked, but melt was still present interstitially. Olivine initially accommodated most of the strain by dislocation creep (Fig. 6e,f). Concomitantly, bending of coarse-grained Pl crystals occurred around more rigid Cpx crystals (Meurer and Boudreau, 1998) and diffusion creep led to grain boundary migration and dissolution/precipitation processes in Pl crystals (e.g., Means and Park, 1994; Nicolas and Ildefonse, 1996; Meurer and Boudreau, 1998). At decreasing melt fraction, and at near solidus conditions when Ol is no longer the weakest phase, Pl also accommodated the strain by dislocation creep, developing subgrain boundaries and mechanical twins (e.g., Meurer and Boudreau, 1998). Therefore, high-temperature intra-crystalline deformation of coarse-grained

595 Ol and Pl likely occurred at hypersolidus conditions when crystals were interlocked and melt
596 was still present in the crystal pile; deformation then proceeded as melt fraction decreased to
597 further deform Pl and, to minor extents, Cpx by dislocation creep.

598   Conversely, fine-grained minerals show no subgrain boundaries (Figs. 4, 6a,b) and have
599 homogeneous and low Mis2Mean, GOS and MGD (Fig. 5). It was also commonly observed in
600 Hole U1473A that fine-grained intervals had better developed magmatic fabrics (MacLeod et
601 al., 2017). This indicates that fine-grained crystals did not record and are not a result of
602 extensive intra-crystalline deformation. The lack of plastic deformation suggests that the
603 observed magmatic fabrics developed when crystal particles were interacting between them,
604 but the crystal matrix was not yet interlocked (e.g., Ildefonse et al., 1992, 1997). This occurred
605 at relatively high melt fractions (at or above ~30-35% melt fraction; e.g., Van der Molen and
606 Paterson, 1979). Suspension flow persists until grains are fully locked, when deformation starts
607 to be accommodated by the crystal matrix. Once the crystal matrix is locked, the magmatic
608 fabric can only be modified by another mechanism such as pressure solution (e.g., Nicolas and
609 Ildefonse, 1996) or plastic deformation. Interestingly, the lack of deformation in the fine-
610 grained crystals indicate that upon crystallization of the fine-grained intervals, the crystal
611 matrix did not accommodate much deformation even after interlocking of the crystal matrix.

612   To summarize, deformation in the coarse-grained intervals occurred under hyper- to near-
613 solidus conditions and at decreasing melt fractions; the strain was accommodated by the crystal
614 framework. Conversely, magmatic fabrics in the fine-grained intervals developed when
615 crystals could interact with each other (at or above 30-35% melt fraction) in suspension flow
616 regime, during which deformation was essentially taken up by the melt fraction. The
617 undeformed character of fine-grained crystals indicate that strain was likely minor during the
618 last stages of crystallization.

619

6.2.2 Pl CPO indicative of crystal mush compaction

621   The scarce occurrence of aligned Pl crystals, resulting in an overall weak or absent Pl
622 SPO, is in agreement with the isotropic to weak magmatic CPO that characterize the studied
623 olivine gabbros (Fig. 1,2). Although magmatic fabrics are weak, as observed at the macroscopic
624 scale and documented by low *J*- and M-indices (Fig. 8), Pl CPO of the fine-grained intervals
625 are characterized by clear patterns that allow a quantitative analysis of the fabrics; magmatic
626 fabrics of coarse-grained intervals are quantified by the calculated parameters (BA- and K-

indices), while visually coarse-Pl CPO are rather random. Due to the tabular shape of Pl crystals, their (010) planes organize parallel to the foliation plane and [100]-axis parallel to the lineation direction (e.g., Morales et al., 2011; Holness et al., 2017; Satsukawa et al., 2013; Vukmanovic et al., 2018; Bertolett et al., 2019). Hence, the foliation and lineation can be recognized in the studied olivine gabbros by preferential distribution of the poles to (010) and [100]-axis, respectively. Based on their symmetry (respective strengths of foliation and lineation), we distinguished two families of Pl CPO that correspond to coarse-grained and fine-grained intervals.

CPO of coarse-grained Pl show rather low BA- and [100] K-indices (Fig. 8b) suggesting very weak foliation and no lineation. On the other hand, fine-grained Pl typically display type-P CPO patterns (classification from Satsukawa et al., 2013; Fig. 7) with intermediate to high BA- (on average ~0.5; Fig. 8a) and [100] K-indices (Fig. 8b), thus indicating weak foliations and lineations. The lineation is overall oriented sub-horizontal respect to the vertical of the drill core (Fig. 7).

The studied olivine gabbros show no evidence of significant crystal-plastic overprinting (Fig. 4), suggesting that their fabrics were not modified during the exhumation event; thus, the documented Pl CPO are representative of the magmatic emplacement process. Contacts between coarse- and fine-grained intervals are irregular and display no clear evidence of cross-cutting relationships. Additionally, mineral geochemistry indicates that melts forming the fine-grained olivine gabbros originated within the associated coarse-grained olivine gabbros, as evidenced by systematically more evolved compositions of fine-grained intervals respect to their coarse-grained counterpart (Ferrando et al., in revision, 2021). Therefore, the grain-size variations showing irregular contacts do not result from multiple melt intrusions but from processes of melt migration and melt extraction within a single crystal mush (see following section; Ferrando et al., in revision). In this scenario, magmatic foliations without well-defined lineations in the coarse-grained olivine gabbros could have developed during crystal accumulation (or settling) or as a consequence of compaction of the crystal pile (or a combination of these two processes). However, the small dimension of magmatic intrusions inferred for the Atlantis Bank OCC (e.g., Dick et al., 2019a), and their fast cooling (John et al., 2004; Coogan et al., 2007), likely hampered the development of foliations by buoyancy-driven crystal settling. This is further supported by the absence of modal layering.

The widespread evidence of intra-crystalline deformation recorded in coarse-grained minerals (subgrain boundaries in Ol and Pl, mechanical twins and bending of Pl crystals, and incipient development of subgrain boundaries in Pl at Pl-Pl and Pl-Cpx contacts; Fig. 3, Fig. 4), together with very weak foliation but no lineation indicate that the crystal mush was deformed by coaxial strain (e.g., Nicolas, 1992; Holness et al., 2017) as the result of compaction. Moreover, the absence of a well-developed SPO (Fig. 10a,b) suggest that compaction was weak in this gabbroic mush (Fig. 10c), in turn suggesting weak strain. The development of compaction-driven foliations was previously documented for Pl in continental gabbroic sequences (e.g., Higgins, 1991; Meurer and Boudreau, 1998; Bertolett et al., 2019) and in other oceanic gabbroic bodies (Satsukawa et al., 2013).

On the other hand, the Pl Type-P CPO patterns observed in the fine-grained intervals (Fig. 7) are typical of foliated rocks with weak to moderate linear fabrics (Satsukawa et al., 2013) that develop in the direction of a magmatic flow (e.g., Brothers, 1964; Benn and Allard, 1989; Higgins, 1991; Nicolas, 1992; Morales et al., 2011). In this context, the orientation of the fabric is a function of the crystal shapes and finite strain (e.g., Ildefonse et al., 1992, 1997). In the studied fine-grained olivine gabbros, the lack of intra-crystalline deformation indicates that strain was accommodated by the high melt fraction during the early stages of magmatic flow and that the crystal matrix remained essentially undeformed during the entire crystallization history (see Section *6.2.1*), in contrast with their coarse-grained counterpart. Given the small scale of the fine-grained intervals and their relatively fast crystallization during the exhumation-related cooling of the system (Ferrando et al., in revision), these intervals likely preserved the fabrics related to magmatic flow. During the early stages of magmatic flow, the high melt fraction allowed elongated Pl crystals to orient in the direction of melt migration, in turn leading to the development of the weak lineations and foliations observed in the fine-grained olivine gabbros.

6.3 Weak compaction and melt accumulation in the U1473A gabbros

In the lower oceanic crust exposed at the Atlantis Bank OCC, upward trends of mineral and bulk-rock geochemical compositions were interpreted as resulting from upward melt migration through a pre-existing crystal mush (Dick et al., 2000, 2019a; Natland and Dick, 2001; Boulanger et al., 2020; Zhang et al., 2020). Specifically, within the studied lower section of IODP Hole U1473A, upward decreasing Mg# (Fig. 1b) and Cr_2O_3 concentrations in Cpx,

690 coupled with decreasing bulk-rock Mg# (Dick et al., 2019b), indicate that porous melt transport

691 was associated with progressive evolution of the migrating melt compositions (Ferrando et al.,

692 in revision). At the scale of crystal aggregates, porous migration and melt geochemical

693 evolution are recorded in large poikilitic Cpx, commonly showing geochemical zonation

694 marked by decreasing compatible elements and increasing trace element contents from crystal

695 cores to rims (Meyer et al., 1989; Gao et al., 2007; Lissenberg and MacLeod, 2016; Boulanger

696 et al., 2020; Sanfilippo et al., 2020; Zhang et al., 2020). Consistently, coarse-grained Pl and

697 Cpx in the studied samples display geochemical zonation (Ferrando et al., 2021) that point to

698 progressive geochemical evolution of the crystallizing magma, at decreasing melt mass.

699 Geochemical mineral compositions suggest that cores of coarse-grained Ol+Pl±Cpx formed a

700 primitive crystal mush, in which the subsequent melt migration occurred (Fig. 10a; Ferrando

701 et al., in revision).

702   The modal composition of poikilitic minerals can be used as a proxy of the crystal mush

703 porosity, since they likely represent the crystallizing products of melt porous migration (e.g.,

704 Meyer et al., 1989; Lamoureux et al., 1999; Coogan et al., 2000; Lissenberg and Dick, 2008).

705 Accordingly, the widespread abundance of poikilitic Cpx (>30% in modal composition on

706 average; Table 1) in the studied coarse-grained intervals suggest that melt migration occurred

707 when an elevated melt fraction was present in the crystal mush (minimum of ~30% melt

708 fraction, i.e., at magmatic and sub-magmatic conditions; see Nicolas, 1992). In this scenario,

709 melt migration was most likely driven by the positive buoyancy of the melts with respect to the

710 crystal framework (e.g., Lissenberg et al., 2019), while compaction of coarse-grained intervals

711 may have had a minor role. This buoyant melt migration was accompanied by crystallization

712 and progressive decrease in porosity, in turn leading to increasing interlocking of crystals.

713   We emphasize that mineral geochemical analyses indicate that coarse-grained minerals

714 show more primitive chemical compositions compared to the fine-grained counterparts

715 (Ferrando et al., 2021). This indicates that the formation of coarse-grained mineral cores

716 occurred prior to crystallization of fine-grained olivine gabbros. Remarkably, fine-grained

717 minerals show homogeneous chemical compositions similar to the rims of the coarse-grained

718 minerals, thus pointing to a genetic relationship between their parental melts (Ferrando et al.,

719 in revision). Based on this genetic relationship, coarse- and fine-grained mineral compositions

720 were interpreted as resulting from partial extraction of the residual melts from the pre-existing

721 coarse-grained crystal mush into discrete crystal-poor zones (Fig. 10c). These horizons, defined

722 as "melt-rich zones" in Ferrando et al., (in revision), were characterized by scarce pre-existing

crystal nuclei, which prevented crystal growth and enhanced nucleation at decreasing temperature to form the fine-grained olivine gabbros. Therefore, the fine-grained intervals represent crystallization products of melts extracted from the coarse-grained crystal mush, generating the textural variability that characterizes the studied rocks (Fig. 10d) and is ubiquitously present throughout Hole U1473A.

This process of melt extraction and accumulation in melt-rich and discrete intervals was promoted by compaction of the coarse-grained crystal mush (Fig. 10c,d), as indicated by the intra-crystalline deformation and the very weak foliation in the coarse-grained olivine gabbros. Lack of well-developed Pl SPO and the occurrence of plastically deformed Ol, Pl and Cpx (Figs. 4, 5) in the weakly foliated coarse-grained olivine gabbros (Figs. 7, 9a) suggest that compaction was most efficient when crystals became interlocked and accommodated the strain (Fig. 10c). Mechanical interactions between grains result in an overall reduction in interstitial volume between crystals, that in turn led to expulsion of the interstitial melts. The chemical similarity between rims of coarse-grained crystals and unzoned fine-grained minerals indicate that a portion of that interstitial melt was retained in the coarse-grained intervals to crystallize the crystal rims, also further suggesting that compaction was relatively weak. In the melt-rich zones, where portions of extracted melts accumulated, the strain was taken up by the melt fraction and the fine-grained crystals were oriented preferentially along the direction of the melt flow, thus developing the observed weak foliations and lineations (Fig. 7, Fig. 8b, Fig. 9a, Fig. 10c).

Combined textural and geochemical constraints indicate that compaction of the crystal pile did not trigger upward melt migration through the coarse-grained crystal mush. Rather, compaction drove local melt extraction and accumulation in crystal-poor intervals, in turn generating local but ubiquitous grain-size variations in the olivine gabbros from the Atlantis Bank OCC.
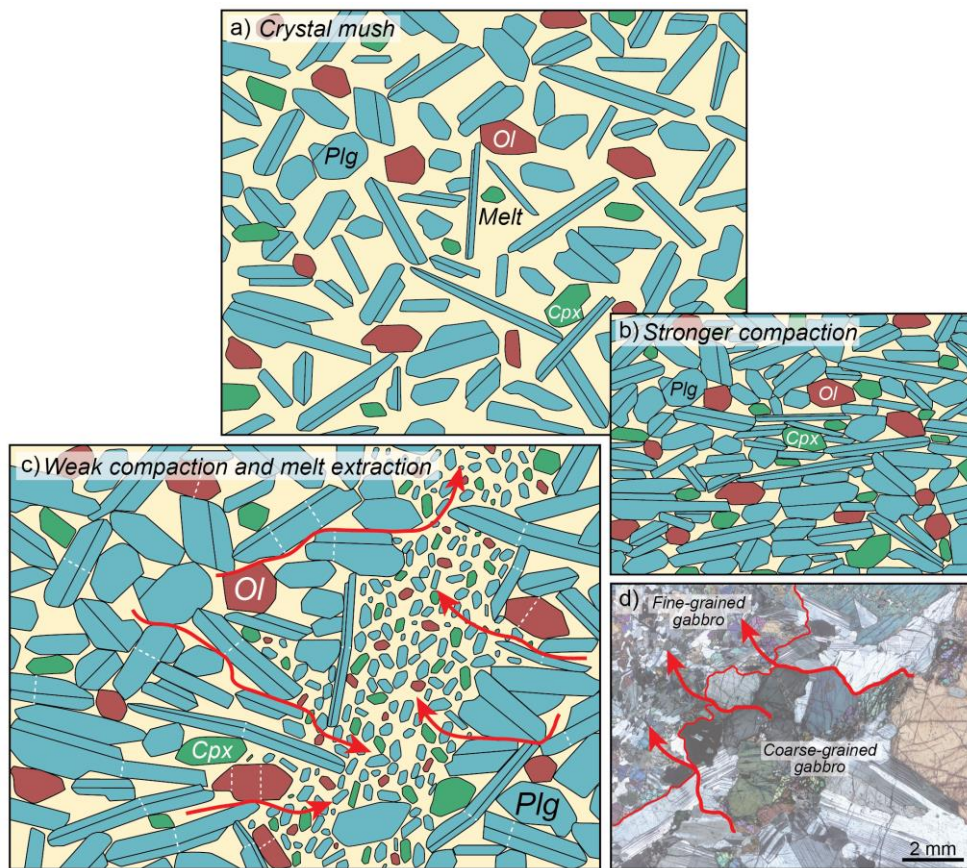
Figure 10: Sketch illustrating the consequence of compaction of a crystal mush (A) at a slow-spreading environment: (B) strong compaction leads to the development of strong foliations, while (C) weak compaction produces very weak foliation. In the case of gabbros from the Atlantis Bank OCC, microstructures and mineral chemistry point to processes of melt migration, extraction and accumulation: (A) in a pre-existing Ol+Pl±Cpx melts buoyantly migrate upward; (C) as crystallization proceeds and porosity decreases, compaction of the crystal pile aides melt extraction and accumulation of melts in discrete zones; (C-D) melt segregates in these discrete zones to finally form the fine-grained intervals observed throughout Hole U1473A.

7. Concluding remarks

At slow to ultraslow-spreading ridges, accretion is mainly accommodated by extensive faulting during discontinuous melt supply, a process that leads to strong crystal-plastic overprint on magmatic textures. Textures of primary magmatic processes are better preserved in the deepest portions of lower oceanic crustal sections observed at slow-spreading ridges. In IODP Hole U1473A at the Atlantis Bank OCC, olivine gabbros from the 500-800 mbsf depth interval preserve microstructural and chemical features of magmatic processes. Microstructural analyses, supported by the previous geochemical study of grain-size variations in these olivine gabbros, provide key evidence of melt migration and subsequent compaction-driven melt extraction in discrete intervals throughout the hole. The origin of heterogeneous grain-sizes in these olivine gabbros can be reconstructed as follows:

(i) Formation of the primitive crystal mush occurred beneath the SWIR axis. Cores of Ol, Pl and minor Cpx grew to form coarse-grained crystals. With more than 30% of melt (corresponding to the mineral modes of clinopyroxene crystallizing from the melt) present between the crystals, buoyancy-driven upward melt migration occurred through the mineral coarse-grained matrix;

(ii) Buoyancy-driven melt migration persisted as porosity and melt fraction decreased. Crystals began to interlock. Weak compaction led to very weak foliation and to deformation of the coarse-grained crystals under dislocation creep (Ol and Pl) and diffusion creep (mainly Pl) mechanisms. This resulted in the documented intra-crystalline deformation features (e.g., subgrain boundaries, bended pl around cpx, undulose extinction of cpx, high GOS and MGD);

(iii) Weak compaction of the coarse-grained crystal pile aided extraction of residual melts from the crystal mush into discrete 'melt-rich zones'. Here, local deformation was taken up by the melt fraction while fine-grained crystals remained undeformed; crystals oriented in the direction of melt transport, developing the observed weak lineation and foliations. High nucleation rates in these zones ultimately formed the fine-grained olivine gabbro.

We here provide an example of slow-spread oceanic crust where compaction is typically weak. Compaction is mainly recorded in the coarse-grained intervals and was identified by intra-crystalline deformation and very weak foliations without the occurrence of lineation. Weak foliations and lineations are instead observed in the fine-grained intervals where deformation likely occurred under coaxial strain with a component of non-coaxial strain. Processes of compaction can produce local, but ubiquitous, chemical and grain-size heterogeneities in a lower crustal section, as those observed in olivine gabbros from the Atlantis Bank OCC. Conversely, compaction had a minor role in the melt movement at larger scales (e.g., the whole crystal mush) within the oceanic crust, which occurred by porous flow, likely driven by positive buoyancy of the melt.

Acknowledgments

References

Allard, M., Ildefonse, B., Oliot, E., 2020. Plastic deformation of plagioclase in a gabbro pluton at a slow-spreading ridge (IODP Hole U1473A, Atlantis Bank, Southwest Indian ridge). AGU Fall Meeting 2020, Abstract n°T026-0011.

Arai, S., Dick, H.J.B., and Scientific Party, 2000. Cruise Report, Mode 2000 (Kairei/Kaiko KR00-06): Yokosuka, Japan (Japanese Agency for Marine-Earth Science and Technology).

Baines, A.G., Cheadle, M.J., Dick, H.J.B., Scheirer, A.H., John, B.E., Kusznir, N.J., Matsumoto, T., 2003. Mechanism for generating the anomalous uplift of oceanic core complexes: Atlantis Bank, Southwest Indian Ridge. Geology 31, 1105–1108. https://doi.org/10.1130/G19829.1

Baines, G.A., Cheadle, M.J., Dick, H.J.B., Scheirer, A.H., John, B.E., Kusznir, N.J., Matsumoto, T., 2007. Evolution of the Southwest Indian ridge from 55°45′E to 62°E: Changes in plate-boundary geometry since 26 Ma. Geochemistry, Geophys. Geosystems 8. https://doi.org/10.1029/2006GC001559

Baines, G.A., Cheadle, M.J., John, B.E., Schwartz, J.J., 2008. The rate of oceanic detachment faulting at Atlantis Bank, SW Indian Ridge. Earth Planet. Sci. Lett. 273, 105–114. https://doi.org/10.1016/j.epsl.2008.06.013

Basch, V., Rampone, E., Crispini, L., Ferrando, C., Ildefonse, B., Godard, M., 2019. Multi-stage reactive formation of troctolites in slow-spreading oceanic lithosphere (Erro − Tobbio, Italy): a combined field and petrochemical study. J. Petrol. 60, 873–906. https://doi.org/10.1093/petrology/egz019

Basch, V., Rampone, E., Crispini, L., Ferrando, C., Ildefonse, B., Godard, M., 2018. From mantle peridotites to hybrid troctolites: textural and chemical evolution during melt-rock interaction history. Lithos 323, 4–23. https://doi.org/10.1016/j.lithos.2018.02.025

Bédard, J. H., 2015, Ophiolitic magma chamber process, a perspective from the Canadian Appalachians. In: Charlier, B, Namur, O., Latypov, R. and Tegner, C. (eds) Layered Intrusions. Springer Geology. Springer, Dordrecht, 693–732. https://doi.org/10.1007/978-94-017-9652-1_15

Bertolett, E.M., Prior, D.J., Gravley, D.M., Hampton, S.J., Kennedy, B.M., 2019. Compacted cumulates revealed by electron backscatter diffraction analysis of plutonic lithics. Geology 47, 445–448. https://doi.org/10.1130/G45616.1

Blackman, D.K., Ildefonse, B., John, B.E., Ohara, Y., Miller, D.J., Abe, N., Abratis, M., Andal, E.S., Andreani, M., Awaji, S., Beard, J.S., Brunelli, D., Charney, A.B., Christie, D.M., Collins,

840   J., Delacour, A.G., Delius, H., Drouin, M., Einaudi, F., Escartín, J., Frost, B.R., Früh-Green,
841   G., Fryer, P.B., Gee, J.S., Godard, M., Grimes, C.B., Halfpenny, A., Hansen, H.E., Harris,
842   A.C., Tamura, A., Hayman, N.W., Hellebrand, E., Hirose, T., Hirth, J.G., Ishimaru, S.,
843   Johnson, K.T.M., Karner, G.D., Linek, M., MacLeod, C.J., Maeda, J., Mason, O.U., McCaig,
844   A.M., Michibayashi, K., Morris, A., Nakagawa, T., Nozaka, T., Rosner, M., Searle, R.C., Suhr,
845   G., Tominaga, M., Handt, A. von der, Yamasaki, T., Zhao, X., 2011. Drilling constraints on
846   lithospheric accretion and evolution at Atlantis Massif, Mid-Atlantic Ridge 30° N. Journal of
847   Geophysical Research 116, B07103. https://doi.org/10.1029/2010jb007931

848   Boulanger, M., France, L., Deans, J., Ferrando, C., Lissenberg, J., von der Handt, A., 2020.
849   Magma reservoir formation and evolution at a slow-spreading center (Atlantis Bank, Southwest
850   Indian Ridge). Front. Earth Sci. 8, 554598. https://doi.org/10.3389/feart.2020.554598

851   Boudier, F., Nicolas, A., Ildefonse, B., 1996. Magma chambers in the Oman ophiolite: fed from
852   the top and the bottom. Earth Planet. Sci. Lett. 144, 239–250. https://doi.org/10.1016/0012-
853   821X(96)00167-7

854   Brothers, R.N., 1964. Petrofabric analyses of Rhum and Skaergaard layered rocks. J. Petrol. 5,
855   255–274. https://doi.org/10.1093/petrology/5.2.255

856   Brown, T.C., Cheadle, M.J., John, B.E., Coogan, L.A., Gee, J.S., Karson, J.A., Swapp, S.M.,
857   2019. Textural character of gabbroic rocks from Pito Deep: a record of magmatic processes
858   and the genesis of the upper plutonic crust at fast-spreading mid-ocean ridges. J. Petrol. 60,
859   997–1026. https://doi.org/10.1093/petrology/egz022

860   Canales, J.P, Dunn, R.A., Arai, R., Sohn, R.A., 2017. Seismic imaging of magma sills beneath
861   an   ultramafic-hosted   hydrothermal   system.   Geology   45,   451–454.
862   https://doi.org/10.1130/G38795.1

863   Cannat, M., Rommevaux-Jestin, C., Sauter, D., Deplus, C., Mendel, V., 1999. Formation of
864   the axial relief at the very slow spreading Southwest Indian Ridge (49° to 69°E). J. Geophys.
865   Res. 104843, 822–825. https://doi.org/10.1029/1999JB900195

866   Cannat, M., Sauter, D., Mendel, V., Ruellan, E., Okino, K., Escartin, J., Combier, V., Baala,
867   M., 2006. Modes of seafloor generation at a melt-poor ultraslow-spreading ridge. Geology 34,
868   605–608. https://doi.org/10.1130/G22486.1

869   Cashman, K.V., Sparks, R.S.J., Blundy, J.D., 2017. Vertically extensive and unstable
870   magmatic   systems: A   unified   view   of   igneous   processes.   Science   355.
871   https://doi.org/10.1126/science.aag3055

872   Cheadle, M.J., Gee, J.S., 2017. Quantitative textural insights into the formation of gabbro in
873   mafic intrusions. Elements 13, 409–414. https://doi.org/10.2138/gselements.13.6.409

874   Coogan, L.A., Jenkin, G.R.T., Wilson, R.N., 2007. Contrasting cooling rates in the lower
875   oceanic crust at fast- and slow-spreading ridges revealed by geospeedometry. J. Petrol. 48,
876   2211–2231. https://doi.org/10.1093/petrology/egm057

877   Coogan, L.A., Saunders, A.D., Kempton, P.D., Norry, M.J., 2000. Evidence from oceanic
878   gabbros for porous melt migration within a crystal mush beneath the Mid-Atlantic Ridge.
879   Geochemistry, Geophys. Geosystems 1. https://doi.org/10.1029/2000GC000072

880 Dick, H.J.B., Kvassnes, A.J.S., Robinson, P.T., MacLeod, C.J., Kinoshita, H., 2019. The
881 Atlantis Bank Gabbro Massif, Southwest Indian Ridge. Prog. Earth Planet. Sci. 6:64.
882 https://doi.org/10.1186/s40645-019-0307-9

883 Dick, H.J.B., Macleod, C.J., Blum, P., Abe, N., Blackman, D.K., Bowles, J.A., Cheadle, M.J.,
884 Cho, K., Ciążela, J., Deans, J.R., Edgcomb, V.P., Ferrando, C., France, L., Ghosh, B.,
885 Ildefonse, B., John, B., Kendrick, M.A., Koepke, J., Leong, J.A.M., Liu, C., Ma, Q., Morishita,
886 T., Morris, A., Natland, J.H., Nozaka, T., Pluemper, O., Sanfilippo, A., Sylvan, J.B., Tivey,
887 M.A., Tribuzio, R., Viegas, G., 2019. Dynamic accretion beneath a slow-spreading ridge
888 segment: IODP Hole 1473A and the Atlantis Bank Oceanic Core Complex. J. Geophys. Res.
889 Solid Earth 124, 2631– 12659. https://doi.org/10.1029/2018JB016858

890 Dick, H.J.B., Meyer, P.S., Bloomer, S., Kirby, S., Stakes, D., Mawer, C., 1991.
891 Lithostratigraphic evolution of an in-situ section of oceanic Layer 3. In: Von Herzen, R.P.,
892 Robinson, P.T., et al., Proc. Ocean Drill. Program, Sci. Results, 118 Coll. Station. TX (Ocean
893 Drill. Program) 439–538. https://doi.org/10.2973/odp.proc.sr.118.128.1991

894 Dick, H.J.B., Natland, J.H., Alt, J.C., Bach, W., Bideau, D., Gee, J.S., Haggas, S., Hertogen,
895 J.G.H., Hirth, G., Holm, P.M., Ildefonse, B., Iturrino, G.J., John, B.E., Kelley, D.S., Kikawa,
896 E., Kingdon, A., LeRoux, P.J., Maeda, J., Meyer, P.S., Miller, D.J., Naslund, H.R., Niu, Y.-L.,
897 Robinson, P.T., Snow, J., Stephen, R.A., Trimby, P.W., Worm, H.-U., Yoshinobu, A., 2000. A
898 long in situ section of the lower ocean crust: results of ODP Leg 176 drilling at the Southwest
899 Indian Ridge. Earth Planet. Sci. Lett. 179, 31–51. https://doi.org/10.1016/S0012-
900 821X(00)00102-3

901 Dick, H.J.B, Schouten, H., Meyer, P.S., Gallo, D.G., Bergh, H., Tyce, R., Patriat, P., Johnson,
902 K.T.M., Snow, J., Fischer, A., 1991. Tectonic evolution of the Atlantis II Fracture Zone. In:
903 Von Herzen, R.P., Robinson, P.T., et al., Proc. Ocean Drill. Program, Sci. Results, 118 Coll.
904 Station. TX (Ocean Drill. Program) 359–398.

905 Dimanov, A., Dresen, G., 2005. Rheology of synthetic anorthite-diopside aggregates:
906 implications for ductile shear zones. J. Geophys. Res. 110.
907 https://doi.org/10.1029/2004JB003431.

908 Dimanov, A., Dresen, G., Wirth, R., 1998. High-temperature creep of partially molten
909 plagioclase aggregates. J. Geophys. Res. 103, 9651–9664. https://doi.org/10.1029/97JB03742

910 Escartín, J., Smith, D.K., Cann, J., Schouten, H., Langmuir, C.H., Escrig, S., 2008. Central role
911 of detachment faults in accretion of slow-spreading oceanic lithosphere. Nature 455, 790–794.
912 https://doi.org/10.1038/nature07333

913 Ferrando, C., France, L., Basch, V., Sanfilippo, A., Tribuzio, R., Boulanger, M., in revision.
914 Grain size variations record segregation of residual melts in slow-spreading oceanic crust
915 (Atlantis Bank, 57°E Southwest Indian Ridge). J. Geophys. Res.: Solid Earth, Special Issue
916 'Ophiolites and Oceanic Lithosphere, with a focus on the Samail ophiolite in Oman', minor
917 revisions, revised manuscript submitted on 27/12/2020.

918 Ferrando, C., France, L., Basch, V., Sanfilippo, A., Tribuzio, R., Boulanger, M., 2021. In situ
919 mineral major, minor and trace element concentrations in olivine, plagioclase and
920 clinopyroxene from olivine gabbros recovered in IODP Hole U1473A at the Atlantis Bank

OCC (57°E, Southwest Indian Ridge), Version 1.0. Interdisciplinary Earth Data Alliance (IEDA). https://doi.org/10.26022/IEDA/111818.

Ferrando, C., Godard, M., Ildefonse, B., Rampone, E., 2018. Melt transport and mantle assimilation at Atlantis Massif (IODP Site U1309): Constraints from geochemical modeling. Lithos 323, 24-43. https://doi.org/10.1016/j.lithos.2018.01.012

Ferrando, C., Lynn, K.J., Basch, V., Ildefonse, B., Godard, M., 2020. Retrieving timescales of oceanic crustal evolution at Oceanic Core Complexes: Insights from diffusion modelling of geochemical profiles in olivine. Lithos 376–377, 105727. https://doi.org/10.1016/j.lithos.2020.105727

Gao, Y., Hoefs, J., Hellebrand, E., von der Handt, A., Snow, J.E., 2007. Trace element zoning in pyroxenes from ODP Hole 735B gabbros : diffusive exchange or synkinematic crystal fractionation ? Contrib. Miner. Pet. 153, 429–442. https://doi.org/10.1007/s00410-006-0158-4

Hess, H.H., 1960. Stillwater igneous complex, Montana: a quantitative mineralogical study. Geol. Soc. America Mem. 80, 230 pp. https://doi.org/10.1130/MEM80

Higgins, M.D., 1991. The origin of laminated and massive anorthosite, Sept Iles layered intrusion, Quebec, Canada. Contrib. Mineral. Petrol. 106, 340–354. https://doi.org/10.1007/BF00324562

Higgins, M.D., 2006. Quantitative textural measurements in igneous and metamorphic petrology. Cambridge University Press, Cambridge, 265 pp. https://doi.org/10.1017/CBO9780511535574

Holness, M.B., Vukmanovic, Z., Mariani, E., 2017. Assessing the role of compaction in the formation of adcumulates: a microstructural perspective. J. Petrol. 58, 643–674. https://doi.org/10.1093/petrology/egx037

Hosford, A., Tivey, M., Matsumoto, T., Dick, H., Schouten, H., Kinoshita, H., 2003. Crustal magnetization and accretion at the Southwest Indian Ridge near the Atlantis II fracture zone, 0–25 Ma. J. Geophys. Res. Solid Earth 108, 1–23. https://doi.org/10.1029/2001JB000604

Ildefonse, B., Arbaret, L., Diot, H., 1997. Rigid particles in simple shear flow: is their preferred orientation periodic or steady-state? J L. Bouchez et al. (eds.) Granite: From Segregation of Melt to Emplacement Fabrics, Kluwer Academic Publishers, 177-185.

Ildefonse, B., Blackman, D.K., John, B.E., Ohara, Y., Miller, D.J., MacLeod, C.J., Abe, N., Abratis, M., Andal, E.S., Andréani, M., Awaji, S., Beard, J.S., Brunelli, D., Charney, A.B., Christie, D.M., Delacour, A.G., Delius, H., Drouin, M., Einaudi, F., Escartin, J., Frost, B.R., Fryer, P.B., Gee, J.S., Godard, M., Grimes, C.B., Halfpenny, A., Hansen, H.E., Harris, A.C., Hayman, N.W., Hellebrand, E., Hirose, T., Hirth, J.G., Ishimaru, S., Johnson, K.T.M., Karner, G.D., Linek, M., Maeda, J., Mason, O.U., McCaig, A.M., Michibayashi, K., Morris, A., Nakagawa, T., Nozaka, T., Rosner, M., Searle, R.C., Suhr, G., Tamura, A., Tominaga, M., von der Handt, A., Yamasaki, T., Zhao, X., 2007. Oceanic core complexes and crustal accretion at slow-spreading ridges. Geology 35, 623–626. https://doi.org/10.1130/G23531A.1

Ildefonse, B., Sokoutis, D., Mancktelow, N.S., 1992. Mechanical interactions between rigid particles in a deforming ductile matrix. Analogue experiments in simple shear flow. J. Struct. Geol. 14, 1253–1266. https://doi.org/10.1016/0191-8141(92)90074-7

Ji, S., Shao, T., Salisbury, M. H., Sun, S., Michibayashi, K., Zhao, W., Long, C., Liang, F., Satsukawa, T., 2014. Plagioclase preferred orientation and induced seismic anisotropy in mafic igneous rocks. J. Geophys. Res. Solid Earth, 119, 8064–8088. https://doi.org/10.1002/2014JB011352.

John, B.E., Foster, D.A., Murphy, J.M., Cheadle, M.J., Baines, A.G., Fanning, C.M., Copeland, P., 2004. Determining the cooling history of in situ lower oceanic crust-Atlantis Bank, SW Indian Ridge. Earth Planet. Sci. Lett. 222, 145–160. https://doi.org/10.1016/j.epsl.2004.02.014

Kelemen, P. B., Aharanov, E., 1998. Periodic formation of magma fractures and generation of layered gabbros in the lower crust beneath oceanic spreading ridges. In Buck, W.R., Delaney, P.T., Karson, J.A. and Lagrabrielle, Y. (Eds.), Faulting and magmatism at mid-ocean ridges. Geophys. Monogr. Ser. 106, American Geophysical Union, 267–289. https://doi.org/10.1029/GM106p0267

Lamoureux, G., Ildefonse, B., Mainprice, D., 1999. Modelling the seismic properties of fast-spreading ridge crustal Low-Velocity Zones: insights from Oman gabbro textures. Tectonophysics 312, 283–301. https://doi.org/10.1016/s0040-1951(99)00183-3

Leuthold, J., Blundy, J.D., Holness, M.B., Sides, R., 2014. Successive episodes of reactive liquid flow through a layered intrusion (Unit 9, Rum Eastern Layered Intrusion, Scotland). Contrib. to Mineral. Petrol. Mineral. Petrol. 168:1021. https://doi.org/10.1007/s00410-014-1021-7

Lissenberg, C.J., Dick, H.J.B., 2008. Melt-rock reaction in the lower oceanic crust and its implications for the genesis of mid-ocean ridge basalt. Earth Planet. Sci. Lett. 271, 311–325. https://doi.org/10.1016/j.epsl.2008.04.023

Lissenberg, C.J., MacLeod, C.J., 2016. A reactive porous flow control on mid-ocean ridge magmatic evolution. J. Petrol. 57, 2195–2220. https://doi.org/10.1093/petrology/egw074

Lissenberg, C.J., MacLeod, C.J., Bennett, E.N., 2019. Consequences of a crystal mush-dominated magma plumbing system: a mid-ocean ridge perspective. Philos. Trans. R. Soc. A 377, 20180. https://doi.org/http://dx.doi.org/10.1098/rsta.2018.0014

Lissenberg, C.J., MacLeod, C.J., Howard, K.A., Godard, M., 2013. Pervasive reactive melt migration through fast-spreading lower oceanic crust (Hess Deep, equatorial Pacific Ocean). Earth Planet. Sci. Lett. 361, 436–447. https://doi.org/10.1016/j.epsl.2012.11.012

MacLeod, C. J., Boudier, F., Yaouancq, G. and Richter, C., 1996. Gabbro fabrics from Site 894, Hess Deep: implications for magma chamber processes at the East Pacific rise. Proc. Ocean Dril. Prog., Scientific Results 147, 317–328.

MacLeod, C.J., Dick, H.J.B., Allerton, S., Robinson, P.T., Coogan, L.A., Edwards, S.J., Galley, A., Gillis, K.M., Hirth, G., Hunter, A.G., Hutchinson, D., Kvassnes, A.J., Natland, J.H., Salisbury, M., Schandl, E.S., Stakes, D.S., Thompson, G.M., Tivey, M.A., 1998. Geological mapping of slow-spread lower ocean crust: a deep-towed video and wireline rock drilling survey of Atlantis Bank (ODP Site 735, SW Indian Ridge). InterRidge News 7(2), 39–43.

MacLeod, C.J., Dick, H.J.B., Blum, P., Abe, N., Blackman, D.K., Bowles, J.A., Cheadle, M.J., Cho, K., Ciazela, J., Deans, J.R., Edgcomb, V.P., Ferrando, C., France, L., Ghosh, B., Ildefonse, B.M., Kendrick, M.A., Koepke, J.H., Leong, J.A.M., Liu, C., Ma, Q., Morishita, T.,

Morris, A., Natland, J.H., Nozaka, T., Pluemper, O., Sanfilippo, A., Sylvan, J.B., Tivey, M.A., Tribuzio, R., Viegas, L.G.F., 2017. IODP Expedition 360. Proc. Int. Ocean Discov. Progr. 360, 1–51. https://doi.org/10.14379/iodp.proc.360.101.2017

MacLeod, C.J., Searle, R.C., Murton, B.J., Casey, J.F., Mallows, C., Unsworth, S.C., Achenbach, K.L., Harris, M., 2009. Life cycle of oceanic core complexes. Earth Planet. Sci. Lett. 287, 333–344. https://doi.org/10.1016/j.epsl.2009.08.016

Mainprice, D., Bachmann, F., Hielscher, R., Schaeben, H., 2014. Descriptive tools for the analysis of texture projects with large datasets using MTEX: strength, symmetry and components, In: Faulkner, D.R., Mariani, E., Mecklenburgh, J. (Eds.), Rock deformation from field, experiments and theory: a volume in honour of Ernie Rutter. Geological Society, London, Spec. Pub. 409. https://doi.org/http://dx.doi.org/10.1144/SP409.8

Matsumoto, T., Dick H.J.B., Cruise A, 2002. In-situ observation of the lower crust and upper mantle lithology in Atlantis Bank, SWIR - results from ABCDE Cruise, EOS, Transactions of the American Geophysical Union, p 83McKenzie, D.P., 1984. The generation and compaction of partial melts. J. Pet. 25, 713–765.

Means, W.D., Park, Y., 1994. New experimental approach to understanding igneous texture. Geology 22, 323–326.

Meurer, W.P., Boudreau, A.E., 1998. Compaction of igneous cumulates part II: compaction and the development of igneous foliations. J. Geology 106, 293–304. https://doi.org/10.1086/516023

Meyer, P.S., Dick, H.J.B., Thompson, G., 1989. Cumulate gabbros from the Southwest Indian Ridge, 54°S-7°16'E: Implications for magmatic processes at a slow spreading ridge. Cont. Min. Petrol. 103, 44-63. https://doi.org/10.1007/BF00371364

Minshull, T.A., Muller, M.R., Robinson, C.J., White, R.S., and Bickle, M.J., 1998. Is the oceanic Moho a serpentinization front? In Mills, R.A., and Harrison, K. (Eds.), Modern ocean floor processes and the geological record. Geological Society Spec. Pub., 148(1), 71–80. http://dx.doi.org/10.1144/GSL.SP.1998.148.01.05

Miranda, E.A., John, B.E., 2010. Strain localization along the Atlantis Bank oceanic detachment fault system, Southwest Indian Ridge. Geochemistry, Geophys. Geosystems 11. https://doi.org/10.1029/2009GC002646

Mock, D., Neave, D. A., Müller, S., Garbe-Schönberg, D., Namur, O., Ildefonse B., Koepke, J., 2020. Formation of igneous layering in the lower oceanic crust from the Samail Ophiolite, Sultanate of Oman. J. Geophys. Res. Solid Earth. https://doi.org/10.1029/2020JB019573

Morales, L.F.G., Boudier, F., Nicolas, A., 2011. Microstructures and crystallographic preferred orientation of anorthosites from Oman ophiolite and the dynamics of melt lenses. Tectonics 30. https://doi.org/10.1029/2010TC002697

Morgan, J.P., Chen, Y.J., 1993. The genesis of oceanic crust: Magma injection, hydrothermal circulation, and crustal flow. J. Geophys. Res. Solid Earth 98, 6283–6297. https://doi.org/10.1029/92JB02650

1042 Muller, M.R., Minshull, T.A., White, R.S., 1999. Segmentation and melt supply at the
1043 Southwest Indian Ridge. Geology 27, 867–870. https://doi.org/10.1130/0091-
1044 7613(1999)027<0867:SAMSAT>2.3.CO;2

1045 Namur, O., Abily, B., Boudreau, A.E., Blanchette, F., 2015. Igneous layering in basaltic
1046 magma chambers, In: Charlier, B., Namur O., Latypov, R., Tegner, C. (Eds.), Layered
1047 intrusions. Springer Geology. https://doi.org/10.1007/978-94-017-9652-1

1048 Natland, J.H., Dick, H.J.B., 2001. Formation of the lower ocean crust and the crystallization of
1049 gabbroic cumulates at a very slowly spreading ridge. J. Volcanol. Geotherm. Res. 110, 191–
1050 233. https://doi.org/10.1016/S0377-0273(01)00211-6

1051 Natland, J.H., Dick, H.J.B., 2002. Stratigraphy and composition of gabbros drilled in ODP
1052 Hole 735B, SW Indian Ridge: A synthesis of geochemical data, In. Natland, J.H., Dick, H.J.B.,
1053 Miller, D.J., Von Herzen, R.P. (eds.), Proc. Ocean Dril. Prog., Scientific Results. College
1054 Station, TX: Ocean Drilling Program. https://doi.org/10.2973/odp.proc.sr.176.021.2002.

1055 Nicolas, A., 1992. Kinematics in magmatic rocks with special reference to gabbros. J. Petrol.
1056 33, 891–915. https://doi.org/10.1093/petrology/33.4.891

1057 Nicolas, A., Boudier, F., France, L., 2009. Subsidence in magma chamber and the development
1058 of magmatic foliation in Oman ophiolite gabbros. Earth Planet. Sci. Lett. 284, 76–87.
1059 https://doi.org/10.1016/j.epsl.2009.04.012

1060 Nicolas, A., Ceuleneer, G., Boudier, F. and Misseri, M., 1988. Structural mapping in the Oman
1061 ophiolites: Mantle diapirism along an oceanic ridge. In: F. Boudier and A. Nicolas (Eds), The
1062 Ophiolites of Oman. Tectonophysics 151, 27-55. https://doi.org/10.1016/0040-
1063 1951(88)90239-9

1064 Nicolas, A., Ildefonse, B., 1996. Flow mechanism and viscosity in basaltic magma chambers.
1065 Geophys. Res. Lett. 23, 2013–2016. https://doi.org/10.1029/96GL02073

1066 Palmiotto, C., Corda, L., Ligi, M., Cipriani, A., Dick, H.J.B., Douville, E., Gasperini, L.,
1067 Montagna, P., Thil, F., Borsetti, A.M., Balestra, B., Bonatti, E., 2013. Nonvolcanic tectonic
1068 islands in ancient and modern oceans. Geochemistry, Geophysics, Geosystems, 14, 10.
1069 https://doi.org/10.1002/ggge.20279

1070 Park, Y., Means, W.D., 1996. Direct observation of deformation processes in crystal mushes.
1071 J. Struct. Geol. 18, 847–858. https://doi.org/10.1016/S0191-8141(96)80017-4

1072 Park Y., Means W.D., 1997. Crystal rotation and growth during grain flow in a deforming
1073 crystal mush. In: Sengupta S. (eds) Evolution of Geological Structures in Micro- to Macro-
1074 scales. Springer, Dordrecht. https://doi.org/10.1007/978-94-011-5870-1_15

1075 Pettigrew, T.L., Casey, J.F., Miller, D.J., et al., 1999. Proceedings of the Ocean Drilling
1076 Program, Initial Reports, 179: College Station, TX (Ocean Drilling Program).
1077 http://dx.doi.org/10.2973/odp.proc.ir.179.1999

1078 Quick, J.E., Denlinger, R.P., 1993. Ductile deformation and the origin of layered gabbro in
1079 ophiolites. Jour. Geophys. Res. 98, 14015–14027. https://doi.org/10.1029/93JB00698

1080 Rampone, E., Borghini, G., Basch, V., 2020. Melt migration and melt-rock reaction in the
1081 Alpine-Apennine peridotites: Insights on mantle dynamics in extending lithosphere. Geosci.
1082 Front. 11, 151-166. https://doi.org/10.1016/j.gsf.2018.11.001

1083 Rioux, M., Cheadle, M.J., John, B.E., Bowring, S.A., 2016. The temporal and spatial
1084 distribution of magmatism during lower crustal accretion at an ultraslow-spreading ridge:
1085 High-precision U–Pb zircon dating of ODP Holes 735B and 1105A, Atlantis Bank, Southwest
1086 Indian Ridge. Earth Planet. Sci. Lett. 449, 395–406. https://doi.org/10.1016/j.epsl.2016.05.047

1087 Rybacki, E., Dresen, G., 2000. Dislocation and diffusion creep of synthetic anorthite
1088 aggregates. J. Geophys. Res. 105, 26017–26036. https://doi.org/10.1029/2000JB900223

1089 Sanfilippo, A., Tribuzio, R., Tiepolo, M., Berno, D., 2015. Reactive flow as dominant evolution
1090 process in the lowermost oceanic crust: evidence from olivine of the Pineto ophiolite (Corsica).
1091 Contrib. to Mineral. Petrol. 170. https://doi.org/10.1007/s00410-015-1194-8

1092 Sanfilippo, A., MacLeod, C.J., Tribuzio, R., Lissenberg, C.J., Zanetti, A., 2020. Early-stage
1093 melt-rock reaction in a cooling crystal mush beneath a slow-spreading mid-ocean ridge (IODP
1094 Hole U1473A, Atlantis Bank, Southwest Indian Ridge). Front. Earth Sci. 8, 473.
1095 https://doi.org/10.3389/feart.2020.579138

1096 Satsukawa, T., Ildefonse, B., Mainprice, D., Morales, L.F.G., Michibayashi, K., Barou, F.,
1097 2013. A database of plagioclase crystal preferred orientations (CPO) and microstructures-
1098 implications for CPO origin, strength, symmetry and seismic anisotropy in gabbroic rocks.
1099 Solid Earth 4, 511–542. https://doi.org/10.5194/se-4-511-2013

1100 Schoolmeesters, N., Cheadle, M.J., John, B.E., Reiners, P.W., Gee, J., Grimes, C.B., 2012. The
1101 cooling history and the depth of detachment faulting at the Atlantis Massif oceanic core
1102 complex. Geochemistry, Geophys. Geosystems 13, 1–19.
1103 https://doi.org/10.1029/2012GC004314

1104 Sinton, J.M., Detrick, R.S., 1992. Mid-Ocean Ridge Magma Chambers. J. Geophys. Res. 97,
1105 197–216. https://doi.org/10.1029/91JB02508

1106 Van der Molen, I., Paterson,M .S., 1979. Experimental deformation of partially-melted granite.
1107 Contrib. Mineral. Petrol. 70, 299-318. https://doi.org/10.1007/BF00375359

1108 VanTongeren, J.A., Hirth, G., Kelemen, P.B., 2015. Constraints on the accretion of the
1109 gabbroic lower oceanic crust from plagioclase lattice preferred orientation in the Samail
1110 ophiolite. Earth Planet. Sci. Lett. 427, 249–261. https://doi.org/10.1016/j.epsl.2015.07.001

1111 Vukmanovic, Z., Holness, M.B., Monks, K., Andersen, J.C.Ø., 2018. The Skaergaard trough
1112 layering: sedimentation in a convecting magma chamber. Contrib. to Mineral. Petrol. 173, 43.
1113 https://doi.org/10.1007/s00410-018-1466-1

1114 Wager, L. R. and Brown, G. M. (1968). Layered Igneous Rocks. Edinburgh: Oliver and Boyd.

1115 Woodcock, N.H., 1977. Specification of fabric shapes using an eigenvalue method. Geol. Soc.
1116 Am. Bull. 88, 1231–1236. https://doi.org/10.1130/0016-
1117 7606(1977)88<1231:SOFSUA>2.0.CO;2

1118   Yaouancq, G., Macleod, C.J., 2000. Petrofabric investigation of gabbros from the Oman
1119   Ophiolite: comparison between AMS and rock fabric. Mar. Geophys. Res. 21, 289–305.
1120   https://doi.org/10.1023/A:1026774111021

1121   Yu, X., Dick, H.J.B., 2020. Plate-driven micro-hotspots and the evolution of the Dragon Flag
1122   melting anomaly, Southwest Indian Ridge. Earth Planet. Sci. Lett. 531, 116002.
1123   https://doi.org/10.1016/j.epsl.2019.116002

1124   Zhang, W.-Q., Liu, C.-Z., Dick, H.J.B., 2020. Evidence for multi-stage melt transport in the
1125   lower ocean crust: the Atlantis Bank Gabbroic Massif (IODP Hole U1473A, SW Indian Ridge).
1126   J. Petrol. egaa082. https://doi.org/10.1093/petrology/egaa082

Declaration of interests

☒ The authors declare that they have no known competing financial interests or personal relationships that could have appeared to influence the work reported in this paper.

☐The authors declare the following financial interests/personal relationships which may be considered as potential competing interests: